# The life cycle of an undular bore and its interaction with a shallow, intense cold front

DANIEL C. HARTUNG[1], JASON A. OTKIN[2], *JONATHAN E. MARTIN[1]

AND DAVID D. TURNER[2]

[1]*Department of Atmospheric and Oceanic Sciences, University of Wisconsin, Madison, Wisconsin*

[2]*Cooperative Institute for Meteorological Satellite Studies, University of Wisconsin, Madison, Wisconsin*

*Submitted to Monthly Weather Review on:*

*08 April 2009*

*REVISED*

*28 July 2009*

RE-REVISED

*29 September 2009*

* *Corresponding author address:* Jonathan E. Martin, Department of Atmospheric and Oceanic Sciences, 1225 W. Dayton St. Rm 1425A, University of Wisconsin-Madison, Madison, WI 53706

Email: jemarti1@wisc.edu

# ABSTRACT

The evolution of an undular bore and its associated wind shift, spawned by the passage of a shallow surface cold front over the southern Plains of the United States, is examined using surface and remote sensing observations along with output from a high resolution numerical model simulation. Observations show that a separation between the wind shift and thermodynamic properties of the front was induced by the formation of a bore over south-central Kansas around 0200 UTC 29 November 2006. By the time the front/bore complex passed through Lamont, OK approximately four hours later, the bore had reached its maximum intensity and its associated wind shift preceded the trailing baroclinic zone by 20 minutes. Within several hours the bore decayed and a cold frontal passage, characterized by a wind shift coincident with thermodynamic properties was observed at Okmulgee, OK. Thus, a substantial transformation in both the structural and dynamical characteristics of the bore as well as its relationship to the parent surface front occurred during a short period of time.

The details of this evolution are examined using output from a fine-scale numerical simulation, performed using the Weather Research and Forecasting (WRF) model. Analysis of the output reveals that as the bore advanced southeastward it moved into a region with a weaker surface stable layer. Consequently, the wave duct that had supported its maintenance steadily weakened resulting in dissipation of the bore. This circumstance led to a merger of the surface temperature and moisture boundaries with the orphaned wind shift, resulting in the cold frontal passage observed at Okmulgee.

# 1. Introduction

The elements of a classical surface cold frontal zone include strong temperature and moisture boundaries coincident with a substantial veering of the horizontal wind and a local minimum in surface pressure. Despite the conceptual appeal of the classical model, frontal passages in the central United States often do not exhibit all of these features. In fact, Hutchinson and Bluestein (1998) showed that the majority (~60%) of their sampled cold frontal passages across the Southern Plains of the United States lacked this classical structure. Instead, many cold fronts exhibit troughs and wind shifts prior to the passage of the temperature and moisture gradients associated with the cold front itself (Tepper 1950; Hutchinson and Bluestein 1998; Schultz 2004; Schultz 2005).

Schultz (2005) reviewed a collection of mechanisms believed responsible for the formation of prefrontal features, including the generation of a prefrontal bore and subsequent gravity waves. A number of prior studies have investigated cases in which a trough or wind shift formed in advance of a cold front in association with a bore (e.g. Haase and Smith 1984; Karyampudi et al. 1995; Koch and Clark 1999; Locatelli et al. 2002b; Sakai et al. 2005). In the present study, we will examine the interaction between a prefrontal bore and its associated surface cold front in order to illustrate the relationship between the bore life cycle and the evolution of the prefrontal features. Here, a cold front is defined as the warm edge of a 3D zone of temperature and moisture contrast that is coincident with a local maximum in vertical vorticity (i.e. a horizontal wind shift). When the warm edge of the temperature and moisture gradients is

not accompanied by a vertical vorticity maximum however, the feature will be referred to as a thermodynamic boundary (TB)[1].

A number of studies have examined the generation of "Morning Glory" bores, which advance along nocturnal inversions and are forced by sea-breeze fronts along the coast of Australia's Gulf of Carpentaria (e.g. Clark et al. 1981; Smith et al. 1982; Smith and Morton 1984; Smith and Page 1985; Noonan and Smith 1986; Menhofer et al. 1997; Menhofer et al. 1997). Recently, Goler and Reeder (2004) were the first to successfully simulate the generation of morning glory waves through the interaction of opposing east- and west-coast sea breezes over the Cape York Peninsula in northeast Australia. Additional observations and model simulations of undular bores, as well as other types of north Australian cloud lines (NACLs) are presented in Goler et al. (2006) and Goler (2009). Other work has focused on the transition between, and differing dynamical properties of gravity currents (i.e. cold pools and gust fronts), gravity waves and bores both in observations and in laboratory experiments (e.g. Simpson 1982; Wakimoto 1982; Wood and Simpson 1984; Crook 1988; Carbone et al. 1990; Rottman and Simpson 1989; Simpson 1997; Haertel et al. 2001). Unlike bores, gravity currents consist of a head dominated primarily by mixing in the form of billows, clefts and lobes (Simpson 1997). Gravity currents can be thought of as transportive systems in which the presence of surface convergence (i.e. a wind shift) is attributed to the transport of mass forward toward the convergence line (Carbone et al. 1990). In general, bores are partially advective and partially propagative in nature (Schultz 2005). More specifically, internal undular bores, which are predominately propagating systems; lack the rear to forward circulation branch ("feeder flow") characteristic of gravity currents (Carbone et al. 1990; Simpson 1997). Bores move faster than a

[1] The term 'thermodynamic boundary' (TB) refers to the warm (leading) edge of what Sanders (1999) referred to as a 'nonfrontal baroclinic zone'.

pure gravity current when the bore strength, defined as the ratio of the bore depth ($d_b$) to the original depth of the stable layer ($h_0$), is greater than 1 (Simpson 1997) (See Appendix Eqn. A1). The reader is referred to Carbone et al. (1990) and Simpson (1997) for a more detailed explanation of the transitional stages between gravity currents, turbulent and undular bores and solitary waves.

A bore is defined as an advancing buoyancy wave phenomena that consists of an initial hydraulic jump (the bore head) formed when a dense airmass (e.g. cold front, thunderstorm outflow, katabatic flow) is introduced into a less dense, 2-layer, stably stratified fluid system (Crook 1988; Smith 1988; Koch et al. 1991; Simpson 1997; Locatelli et al. 1998; Koch and Clark 1999; Schultz 2005; Koch et al. 2008a). The stable layer, whether elevated or at the surface, must be located beneath a less stable (e.g. neutral or conditionally unstable) layer of sufficient depth to allow the combination to form an efficient wave duct that prevents the vertical propagation of wave energy out of the stable layer (Lindzen and Tung 1976; Crook 1988; Smith 1988; Koch and O'Handley 1997; Locatelli et al. 1998) (Fig. 1). If the bore strength is between 1 and 2, laboratory experiments show the bore to be smooth and non-turbulent (Rottman and Simpson 1989; Simpson 1997). As the depth of the stable layer increases following the passage of the bore such that $2 < d_b/h_0 < 4$, the bore transitions to a more turbulent state as mixing develops along the stable layer downstream of the bore head (Rottman and Simpson 1989; Simpson 1997). If the bore strength is greater than 4, all undulations are eradicated as mixing dominates the motion of the phenomena; resulting in the bore appearing more like a gravity current. However, bores have also been found to behave like gravity currents when their strength is greater than 2 (Rottman and Simpson 1989; Simpson 1997).

At the surface, bores generate a distinct pressure jump followed by a continuous rise in surface pressure and a wind shift toward the direction from which the bore is approaching (Koch et al. 1991; Mahapatra et al. 1991; Simpson 1997; Locatelli et al. 1998; Koch and Clark 1999). Surface warming is often observed coincident with bore passage, a result of the downward mixing of warm, dry air from above the stable layer (i.e Koch and Clark 1999). Koch et al. (2008a) showed that ascent within a bore can also transport moisture upward through the entire depth of the bore, which can result in substantial vertical mixing of low-level moisture. For a more in-depth description of bore wave theory see Koch et al. (1991), Locatelli et al. (1998), or Koch and Clark (1999) and for wave duct theory see Lindzen and Tung (1976). The present case study focuses on an internal undular bore, in which the transitions in height and velocity perturbations in the fluid ahead of the thermodynamic boundary occur over several laminar, wavelike undulations.

In order for an environment to be favorable for bore growth and maintenance in the presence of vertical wave propagation, a strong wave-ducting mechanism must exist (Crook 1988; Koch and Clark 1999). According to Koch and Clark (1999), the presence of a wave duct is supported by a layer characterized by a negative Scorer parameter $m^2$, where $m$ is the vertical wavenumber and

$$m^2 = \frac{N_m^2}{(U - C_{bore})^2} - \frac{\partial^2 U / \partial z^2}{(U - C_{bore})} - k^2 \qquad (1)$$

where $N_m{}^2 = \left[ (g/\theta_v) \partial \theta_v / \partial z \right]$ is the square of the moist Brunt-Vaisala frequency, $\theta_v$ is the virtual potential temperature, $U$ is the ambient wind speed in the direction of the bore movement and $C_{\text{bore}}$ is the phase speed of the bore. The first term in (1) measures the effects of moist static energy (Koch and Clark 1999) while the second term measures the effect of wind profile curvature such as that associated with a low-level jet (LLJ) (Crook 1988; Koch and Clark 1999).

Studies by Crook (1986) and Crook (1988) used numerical simulations to study the effects of wind shear on the vertical trapping of wave energy. When a generation mechanism (e.g. a density current) is introduced into an environment in which 1) a weakly stratified layer sits atop a low-level stable layer, and 2) upper-level flow opposes the wave motion, wave energy is trapped in the stable layer (Crook 1986). This particular trapping mechanism is diagnosed in (1) as an increase in $\left(U - C_{bore}\right)^2$ (and hence a decrease in $m^2$) with height. Crook (1988) showed that the existence of a LLJ opposing the wave motion within the highly stratified surface layer can also lead to substantial trapping of wave energy within the layer. The influence of the LLJ is diagnosed in (1) by the curvature term $\left(\frac{\partial^2 U}{\partial z^2}\right)$ (Crook 1988), which is negative above the LLJ core. So long as a component of the ambient flow is opposite to the movement of the bore, $\left(U - C_{bore}\right)$ is also negative above the LLJ core. This combination results in $m^2$ changing sign from positive to negative above the jet as well. Finally, the last term in (1), the square of the zonal wavenumber *k*, can be ignored because the horizontal length scale of the waves of interest is very large (~ 10 km) (Koch and Clark 1999). The reader is referred to Koch and Clark (1999) for a full description of each term in (1) and Scorer (1949) for a full explanation of the Scorer parameter.

To the best of our knowledge, no prior research has documented the role of the life cycle of a prefrontal bore in governing the interaction between the prefrontal wind shift generated by the bore and the parent cold front. We focus on an intense cold frontal passage over southwest Kansas and central Oklahoma that spawned an undular bore that subsequently moved through southwest Kansas and Oklahoma on 29 November 2006. The main objective of this paper is to document the evolution of the long-lived, bore-induced wind shift and the nature of its

interaction with the parent cold front using a combination of high resolution surface and remotely-sensed observations, along with output from a very high resolution numerical simulation of the event. The paper is structured as follows. Section 2 briefly describes the various datasets used in this analysis and outlines the configuration of the high-resolution numerical model simulation used to enhance the diagnosis of this case. A synoptic overview of the setting in which the event occurred is given in section 3 with analyses of the high-resolution observational datasets presented in section 4. Results from the numerical model simulation are presented in section 5. A discussion of results and concluding remarks are given in section 6.

## 2. Data and Methods

*a. Instrumentation*

Interrogation of the 3-D structure and evolution of the cold front draws upon a number of observational datasets. High spatial and temporal resolution surface observations from the Oklahoma Mesonet and Atmospheric Radiation Measurement (ARM) Surface Meteorological Observation System (SMOS) stations are employed, in addition to remote sensing observations taken from the Raman lidar and the Millimeter wavelength Cloud Radar (MMCR). In 2006, the Oklahoma Mesonet consisted of 122 observing sites distributed across all of Oklahoma. Temperature and relative humidity at 1.5 m above ground level (AGL), barometric pressure (hPa), and wind speed (m $s^{-1}$) and direction at 10 m AGL were all considered in the analysis of this case. Measurements were taken every 3 s with the exception of barometric pressure which was measured every 12 s and then averaged over a 5-minute period. Fifteen SMOS stations in south-central Kansas and north-central Oklahoma were also available for this study. Data from

these sites include temperature, wind speed and direction at 2 m AGL, barometric pressure at 1 m AGL, and precipitation (mm), all of which were recorded at 1-minute intervals. The Oklahoma Mesonet and SMOS data were used to calculate water vapor mixing ratio from the measured temperature, barometric pressure and relative humidity.

The Raman lidar is a water vapor profiling remote sensing tool located at the ARM Southern Great Plains (SGP) Climate Research Facility (CRF) site near Lamont, Oklahoma (Goldsmith et al. 1998, Turner and Goldsmith 1999, Turner et al. 2000). The measured water vapor mixing ratio profiles for this event have a vertical resolution of 75 m beginning at 60 m AGL and are recorded every 10 seconds; this performance was a result of a substantial instrument upgrade in 2004 (Ferrare et al. 2006, Newsom et al. 2009). The random error in the water vapor mixing ratio data at this resolution is << 10% in the planetary boundary layer (PBL). A full detailed description of the Raman lidar can be found in Goldsmith et al. (1998).

Finally, the MMCR is a zenith pointing cloud radar, also located at Lamont, which operates at a frequency of 35-GHz (Moran et al. 1998). At the time of this event, the MMCR was being operated in the so-called "boundary layer" mode (Kollias et al. 2007), which provided enhanced sensitivity to weak cloud echoes (Clothiaux et al. 1999). This mode has a vertical resolution of 45 m, a minimum / maximum range of 105 m / 4920 m, a Nyquist velocity of 5.27 m $s^{-1}$, and an averaging period of 4 s with data collected every 2 s. The present analysis employs the Doppler capability of the MMCR to measure vertical velocity of cloud particles and clutter (e.g. insects) in the boundary layer.

*b. WRF model simulation configuration*

Version 2.2 of the WRF model was used to perform a high-resolution simulation of the formation and evolution of the undular bore associated with the surface cold front. The simulation was initialized at 1800 UTC 28 November 2006 using 0.5º Global Forecast System (GFS) analyses and was integrated for 30 hours on two nested domains containing 5 km and 1 km horizontal grid spacing, respectively (Fig. 2). One-way nesting was used during the simulation so that simulated atmospheric fields from the outer 5 km domain provided lateral boundary conditions for the higher resolution inner domain. The model topography for the inner domain was initialized using the 30 s (~1 km) United States Geological Society topography dataset. The simulation contained 66 vertical levels with the model top set to 10 hPa. The vertical resolution decreased from 50-100 m in the lowest 1 km to ~440 m from 7 km to the model top. Sub-grid scale processes were parameterized using the Thompson et al. (2006) mixed-phase cloud microphysics scheme, the Mellor-Yamada-Janjic planetary boundary layer scheme (Mellor and Yamada 1982), and the Dudhia (1989) shortwave and Rapid Radiative Transfer Model (RRTM) longwave (Mlawer et al. 1997) radiation schemes. Surface heat and moisture fluxes were calculated using the Noah land surface model (LSM). No cumulus parameterization scheme was used; therefore, all clouds were explicitly predicted by the microphysics scheme.

## 3. Synoptic Overview

During the last week of November 2006, an intense surface cold front developed over the Southern Plains of the United States in association with a mature surface cyclone over the northern Great Lakes. In this section, the larger synoptic-scale environment within which the

mesoscale features developed is presented. The analysis employs the 40 km gridded analyses of NCEP's Eta model and specifically focuses on three time periods: 0000 UTC and 1200 UTC 29 November and 0000 UTC 30 November 2006.

At 0000 UTC 29 November, a surface low-pressure center was located over northern Minnesota (not shown). A strong surface cold front, evident in the 950 hPa potential temperature (θ) field, extended from the sea-level pressure (SLP) minimum southwestward across Iowa and Kansas (Fig. 3a). This feature was characterized by a fairly intense temperature gradient at 850 hPa (Fig. 3b). A second SLP minimum was centered over the Oklahoma/Texas panhandles (Fig. 3a), downstream of an upper trough axis centered over the Four Corners region of the southwest United States (Fig. 3c). The weak SLP trough through Oklahoma and Texas, coincident with an axis of maximum 950 hPa θ (Fig. 3a) and absolute vorticity (not shown), was a drytrough as described by Martin et al. (1995) – a leeside trough characterized by a strong moisture contrast. The leeside origin of the drytrough and weak surface cyclone is consistent with the analysis of cold fronts with prefrontal wind shifts offered by Schultz (2004). The middle-tropospheric flow at 500 hPa downstream of the upper trough axis was uniformly from the southwest (Fig. 3c) which led to the importation of an elevated mixed layer (EML) over north-central Oklahoma (not shown).

By 1200 UTC, the primary surface cyclone had progressed northeastward to southwestern Ontario, while the θ gradient associated with the surface frontal zone had nearly doubled in intensity (Fig. 4a). The surface cold front had overtaken the drytrough through Kansas by this time though the features were still separate throughout most of Oklahoma (Fig. 4a). A notable intensification of the 850 hPa temperature contrast had also occurred (Fig. 4b), particularly over the northern Texas panhandle where only a remnant of the weak surface

cyclone from the earlier time existed (Fig. 4a). The flow at 500 hPa remained southwesterly over the central United States as an upper-level short wave approached the base of the large-scale trough axis over the Four Corners region (Fig. 4c).

By 0000 UTC 30 November 2006, as the primary surface cyclone progressed farther to the north over Ontario, the surface frontal zone, as well as its vertical extension at 850 hPa, continued to move across northern Texas and Oklahoma (Figs. 5a,b). The 500 hPa trough continued to deepen while southwesterly flow prevailed over the central United States (Fig. 5c). Interestingly, though the evolution of the surface field in the present case bears similarity to the composite in Schultz (2004) (see his Fig. 12), the same cannot be said about the flow evolution in the middle troposphere (see his Fig. 10). Throughout the entire 24-hour period, the flow remained uniformly southwesterly atop the shallow surface frontal zone, resulting in a nearly 2-D flow field aloft parallel to the surface front (Figs. 3, 4, 5).

## 4. Results

*a. Surface-based observations of the frontal passage*

Surface and remotely sensed observations at stations located in southwest Kansas and north-central and east-central Oklahoma are used to examine the characteristics of the cold front and bore as they passed through the region. Figure 2 shows the location of the stations chosen for observational analysis based on their proximity to the model cross-sections that will be discussed in Section 5. The Larned station is located in southwest Kansas at an elevation of 632 m above sea level (ASL). Lamont is located in north-central Oklahoma, approximately 305 m ASL and Okmulgee (elevation 209 m) is located 185 km to the southeast of Lamont.

*i. Larned, Kansas*

At the Larned, Kansas SMOS station, the observed cold-frontal passage on 28 November 2006 exhibited a nearly classical structure (Fig. 6). Between 2352 UTC and 2357 UTC, a temperature drop of ~3°C (Fig. 6a) and a moisture increase of 0.5 g $kg^{-1}$ (Fig. 6b) were observed nearly coincident with a horizontal wind shift of 170° (Fig. 6c). The increase in moisture following the frontal passage testifies to the dryness of the air behind the drytrough identified in Section 2 (Fig. 3). A slight depression in surface pressure was observed with the frontal passage (Fig. 6d), while the more gradual trend of increasing pressure at the station is consistent with the departure to the south of the weak surface cyclone (e.g. Schultz 2004). As the cold front continued to move to the southeast over the surface observation networks of Kansas and Oklahoma, a deviation from this structure became evident.

*ii. Lamont, Oklahoma*

In contrast to the cold frontal passage at Larned, a pressure minimum was recorded 53 minutes prior to the abrupt temperature and moisture decreases at Lamont (Figs. 7a, b, d). Approximately 10 minutes after the pressure minimum was recorded, the winds began to veer from due south (180°) at 0811 UTC to southwest (190°) by 0834 UTC (Fig. 7c), and then underwent an abrupt 113° shift to northwesterly flow during the next 7 minutes (Fig. 7c). This abrupt wind shift, combined with a coincident 1 hPa spike in surface pressure at 0834 UTC (Fig. 7d), is indicative of a bore passing over the station. Following the passage of the bore, the surface winds continued to shift from northwesterly to a more northerly direction over the subsequent 22 minutes between 0841 and 0903 UTC (Fig. 7c), while a continuous rise in surface

pressure was also observed during the ensuing 2 hour period (Fig. 7d). The TB passage at Lamont, marked by a nearly simultaneous drop in temperature and mixing ratio (4.5°C and 3.5 g $kg^{-1}$, respectively, in the subsequent 10 minutes) occurred at 0853 UTC, 19 minutes after commencement of the bore passage (Figs. 7a, b). Taken together, the observed features are not consistent with a cold frontal passage since the temperature and moisture decreases were not observed simultaneously with the abrupt wind shift. Instead, a bore induced pressure jump and wind shift were observed prior to the actual passage of the TB (Figs. 7c, d).

The SMOS surface observations at Lamont show that a bore was responsible for the wind shift that trailed the leading SLP trough and that both of these non-classical features were observed in advance of the TB (Fig. 7). The sharp 113° wind shift to northwesterly flow recorded at 0834 UTC represents a wind shift to the direction from which the bore was coming (Fig. 7c); a commonly observed characteristic of such phenomena. In agreement with the last of the three bore criteria discussed by Mahapatra et al. (1991), weak surface warming (~0.5°C) was also observed at Lamont around 0834 UTC, coincident with the bore passage (Fig. 7a, b).

The bore signature identified in the surface observations was also evident in an array of remotely sensed observations at the Lamont ARM site. MMCR Doppler vertical velocity observations detected two distinct undulations, the second of which was the most intense, ahead of the surface TB between 0830 and 0900 UTC (Fig. 8a). Simpson (1997) showed that the waves that comprise a soliton are typically amplitude ordered; therefore the first undulation in Fig. 8a is believed to be the bore, while the more intense second undulation is believed to be the thermally direct vertical circulation associated with frontogenesis (not shown). Ascending regions were on the order of 2-4 m $s^{-1}$ while descending regions were a much weaker 1-2 m $s^{-1}$ (Fig. 8a).

The water vapor mixing ratio profile from the Raman lidar reveals a shallow moist layer near the surface with a sharp transition to much drier air above 0.5 km ahead of the bore (Fig. 8b). Shortly after 0830 UTC, the top of the moist layer became slightly elevated coincident with the intrusion of the bore head out ahead of the surface TB (Fig. 8b). After the initial undulation passed the station (first arrow on Fig. 8b), the surface mixing ratio decreased (Fig. 8b), presumably as a consequence of mixing by the bore circulation as suggested by Koch et al. (2008a). The minimal surface drying (0.5 g $kg^{-1}$) observed approximately 3 minutes after the bore signature at the Lamont SMOS station (Fig. 7b) is reflected in Fig. 8b as a slight decrease in water vapor mixing ratio following the passage of the leading ascent region of the bore. As the top of the shallow surface moist layer was lifted from 0.5 to ~0.75 km AGL with the passage of the bore, the associated adiabatic cooling was reflected in a slight decrease in surface temperature (Fig. 7a). In agreement with Koch et al. 2008, the result is a disturbance of the previously tranquil (well-mixed) surface fluid at the head of the thermodynamic boundary. Low-level moisture was lifted further with the passage of the TB, which is marked by the strong horizontal gradient in mixing ratio observed by the sensor shortly before 0900 UTC (Fig. 8b). Comparison of the MMCR Doppler velocities and the calculated vertical displacement of the 10.5 g $kg^{-1}$ mixing ratio isopleth in the Raman lidar data between 0830 UTC and 0838 UTC (not shown) yielded nearly identical vertical velocities increasing from +0.5 m $s^{-1}$ to 2 m $s^{-1}$ with the passage of the bore head. These observations are consistent with those in Koch et al. (2008b) who found that lidar-derived vertical motions within a soliton agreed well with those deduced from height changes in DIAL (Differential absorption lidar) mixing ratio surfaces. Black attenuation spikes above 0.5 km, visible after passage of the first undulation, indicate the presence of optically thick clouds which the laser is unable to penetrate (Fig. 8b). A calibration

of the lidar conducted at 0925 UTC is also reflected in Fig. 8b as a brief slot of dry air at that time. Therefore, the remotely-sensed observations fully support the existence of an undular bore ahead of the surface TB at Lamont. The time at which the lead wave was observed also coincides very well with the observed abrupt (113°) wind shift at the station (Fig. 7c).

*iii. Okmulgee, Oklahoma*

At 1648 UTC, a weak surface pressure trough characterized by a subsequent gradual wind shift from SSE (162°) to SSW (198°), was observed at Okmulgee (Figs. 9c, d). Beginning 17 minutes later (1705 UTC), 10-minute temperature and mixing ratio decreases of 6.5°C and 3.5 g $kg^{-1}$, respectively, (Figs. 9a, b) were observed coincident with an abrupt wind shift from SSW (198°) to W (277°) (Fig. 9c). Recall that the wind shift at Lamont preceded the passage of the TB by approximately 20 minutes. Therefore, in contrast to the situation at Lamont, only a pressure trough, the weak drytrough feature highlighted in Section 3, preceded the cold frontal passage at Okmulgee. The absence of a preceding wind shift and pressure jump at Okmulgee testifies to the absence of a distinct bore signature in the observations at this time.

*(b) Analysis of pre-bore environment*

A sounding taken at 0532 UTC 29 November 2006 at Lamont shows the ambient conditions present prior to the passage of the bore / TB system at the station (Fig. 10). A strong nocturnal inversion (5.8°C) extending from the surface to 922 hPa was present directly beneath an EML that extended to 676 hPa (Fig. 10). Strong directional wind shear is also evident with nearly due south winds at the surface and southwesterly flow aloft in the elevated mixed layer (Fig. 10). A critical level, defined as the level at which the mean flow opposing the wave motion

is equal to the phase speed of the ducted waves[2], was located within the lower portion of the EML directly above the surface stable layer (Table 1). The observed environment allowed for wave energy to be contained in the conditionally unstable layer, greatly increasing wave reflectivity along the boundary between the stable layer and EML and not allowing energy loss from the system (Lindzen and Tung 1976). Finally, based on laboratory experiments detailed in Section 1, the estimated bore strength of 1.72 from observations at Lamont implies that the bore was smooth and non-turbulent at that time (Table 1) (Rottman and Simpson 1989; Simpson 1997).

In summary, the surface observations from the Larned, Lamont and Okmulgee SMOS stations demonstrate that a pressure trough, wind shift and TB moved across Kansas and Oklahoma from northwest to southeast on 28-29 November. The Larned station recorded a cold frontal passage at 2357 UTC 28 November with the temperature and moisture changes observed coincident with the wind shift (Fig. 6). At Lamont a bore signature in the form of a sharp wind shift and pressure jump was observed at 0834 UTC after the passage of a drytrough at ~0800 UTC, and ~20 minutes prior to the passage of the TB (Fig. 7). At Okmulgee, the TB and wind shift were coincident again (i.e. a cold front) at 1705 UTC with a pressure minimum preceding this passage by 15 minutes (Fig. 9). While there were no indications of a bore in the Larned and Okmulgee observations, a considerable evolution in the relationship between the bore and its parent surface cold front in the interval between passage at Lamont and Okmulgee is evident. A numerical model simulation is employed next in order to investigate the evolution of the bore, wind shift, thermodynamic boundary and wave duct between Larned, Lamont and Okmulgee.

[2] Since available observing stations in Oklahoma were not positioned in a line perpendicular to the movement of the bore / TB system, precise calculation of the speed of the bore from surface observations was intractable. Therefore, the calculated speed of the TB was used as an approximation of the speed of the bore in the calculation of the critical level.

## 5. Analysis of the model simulation

In this section, results from the high-resolution WRF model simulation will be used to more closely examine the structural evolution of the bore-induced features identified in the Lamont observations. Inspection of Fig. 11, which shows the evolution of the vertical velocity field at 1 km ASL, reveals that the strength and horizontal extent of the bore and associated soliton varied greatly as these features moved across Kansas and Oklahoma. At 0030 UTC, a vertical circulation associated with lower tropospheric frontogenesis (not shown) is evident in the vertical motion field at 1 km ASL (Fig. 11a). By 0500 UTC, a narrow band of ascent ($w > 1$ m $s^{-1}$) associated with the leading edge of the bore extended ~500 km from southwestern to northeastern Kansas (Fig. 11b). Over the next 3 hours, the bore evolved into a soliton with two distinct undulations over north-central Oklahoma, noted by the advancement of the wave packet ahead of the surface TB (region A) (Fig. 11c). By 1100 UTC (Fig. 11d), however, the soliton had decayed over north-central Oklahoma (region B) while a smaller, locally intense wave packet had developed over west-central Oklahoma (region C). Wind barbs at 500 m ASL support the presence of a southerly LLJ that intensifies from 10 to 15 m $s^{-1}$ on its western flank south of Lamont in central Oklahoma between 0030 and 0800 UTC (Figs. 11a-c). Primary cross-sections analyzed in the next section (along the grey lines in Fig. 11) capture the general SE movement of the bore / TB system across south-central Kansas and Oklahoma between 0030 and 1400 UTC.

*(a) Evolution of Bore / TB System*

Figure 12 contains a series of vertical cross-sections (taken along line *i-ii* in Fig. 11) showing the evolution of the thermal, moisture, wind and Scorer parameter fields as the cold front approached and passed through central Kansas. At 0030 UTC, the temperature and moisture boundaries were coincident with the surface wind shift, signifying a cold frontal structure (Fig. 12a, b). At the leading edge of the cold front (denoted by the 290 K isentrope), a strong updraft coupled with a weak region of descent to the northwest, comprised the thermally direct vertical circulation associated with lower tropospheric positive frontogenesis (not shown). The frontal zone was located within a layer characterized by uniformly positive Scorer parameter values at this time (Fig. 12c). The immediate prefrontal environment was characterized by a shallow surface stable layer with very weak flow opposing the motion of the front (Fig. 12c). Such an environment permits free vertical propagation of wave energy generated by the cold front and is not conducive to bore formation.

As the surface cold front moved into south-central Kansas by 0200 UTC, a small wave packet and a distinct wind shift were evident near its leading edge (Fig. 12d), which was beginning to encroach upon a shallow layer of low-level moisture over north-central OK (Fig. 12e). Two distinct vertical circulations were now evident with the initial circulation associated with the bore while the second circulation was tied to surface frontogenesis (not shown) (Fig. 12d). The cold frontal structure observed in the earlier cross-section had, by this time, evolved into a distinct TB trailing a bore-induced wind shift (Fig. 12d). The immediate prefrontal environment was characterized by a shallow stably stratified surface layer ($\frac{\partial \theta}{\partial z} > 0$) lying beneath a neutrally-stratified layer ($\frac{\partial \theta}{\partial z} = 0$) between 500 and 2000 m AGL (Fig. 12d). The bore / TB system had also encroached upon a LLJ in the stably-stratified layer with an along cross-

section component of ~9 m $s^{-1}$ toward the TB at 400 m AGL by this time (Fig. 12d). The presence of a neutral layer atop a stable layer, combined with the wind-profile curvature associated with the LLJ, (Fig. 12d) comprised the weak wave duct in this region ahead of the surface TB. A critical level ($U = c_{bore}$) was present at ~550 m AGL ahead of the TB at the base of the EML (Fig. 12f). The duct was marked by an abrupt transition to negative Scorer parameter values at ~500 m AGL at the leading edge of the initial wave, indicative of favorable conditions for the trapping of wave energy, and was therefore supportive of wave growth and maintenance (Fig. 12f).

During the next 3 hours, a well-defined bore head developed at the leading edge of the wave packet with a series of low-amplitude waves trailing behind the head at a slightly higher altitude (Fig. 13a). A pronounced wind shift was located at the leading edge of the bore (Fig. 13a), ahead of the surface TB. The coincidence of the leading edge of the bore with the wind shift suggests that the latter was tied to the development of the bore. By this time, the circulation associated with the wave packet began to lift low-level moisture over the leading edge of the TB, similar to the cold frontal case analyzed by Koch et al. (2008a) (Fig. 13b). A strengthening of the ambient wave duct ahead of the bore was observed between 0200 UTC and 0500 UTC as the surface stable layer intensified (Fig. 13a). As the bore / TB system encroached upon the western edge of the LLJ, the wind-profile curvature $\left(\frac{\partial^2 U}{\partial z^2}\right)$ increased, resulting in a critical level at ~0.4 km AGL, at the base of a deep layer of negative Scorer parameter (Fig. 13d). The layer of negative Scorer parameter indicated a strong wave duct ahead of the bore / TB system at this time (Fig. 13c). Finally, between 0200 UTC and 0500 UTC, a substantial increase in mixing ratio in the surface stable layer occurred ahead of the TB (compare Figs. 12e, 13b).

By 0800 UTC the bore reached its maximum intensity (w = +3 m $s^{-1}$ / -2.5 m $s^{-1}$) just prior to passing through Lamont (Fig. 13d). The wind shift and the leading edge of the soliton were located even farther ahead of the surface TB at this time than before. The soliton, which consisted of a very distinct bore head followed by two smaller amplitude waves, induced substantial mixing across the upper portion of the PBL with an 8 g $kg^{-1}$ horizontal mixing ratio gradient across the bore head (Fig. 13e). Though the surface stable layer had weakened slightly by this time (Figs. 13d, f), an ambient wave duct was still present across the region. This was partly a consequence of an ~8 m $s^{-1}$ wind component opposing the bore motion at the base of the EML above the LLJ core (Fig. 13f). The presence of a weaker wave duct at 1.5 km AGL (Fig. 13f) is related to the presence of a weak inversion above the EML in the Lamont sounding (see Fig. 10), as well as the increased speed of the flow opposing the wave motion at 1.5 km AGL (Fig. 13f) (Crook 1988). Figure 13d shows the increased depth of the pre-TB stable layer ($\frac{\partial \theta}{\partial z} >$ 0) that resulted from the passage of the bore (compare the elevation of the 300 K θ isentrope ahead of and behind the initial wave in Fig. 13d). Such a deepening of the stable layer behind the bore head has been shown in observations and in laboratory experiments to be a common feature of such phenomena (e.g. Simpson 1997; Koch and Clark 1999; Koch et al. 2008a).

Lastly, Fig. 14 contains a sequence of cross-sections (along line *iv*-*v* in Fig. 11) showing the evolution of the bore / TB system as it approached and subsequently passed through Okmulgee, OK. Between 0800 UTC and 1100 UTC, the bore moved through a region characterized by a weakening nocturnal inversion (compare Figs. 13d, 14a). As the boundary layer deepened and the near-surface static stability weakened in concert with a persistent wave-normal component of the LLJ (favorable for wave trapping), the critical level ahead of the TB resided *within* the region of weak low-level stratification rather than above it. Such an

environment supports evanescent gravity waves (Lindzen and Tung 1976), and was therefore accompanied by an erosion of the wave duct. This suggests that in the primary cross-sections analyzed here, the rapid decrease in low-level stratification ultimately led to the demise of the ambient wave duct (Fig. 14c). A deepening of the moist surface layer to 1.25 km AGL also occurred in the conditionally unstable region ahead of the TB (Fig. 14b). Without a sufficient wave duct to trap the wave energy below the critical level (Fig. 14c), the bore had decayed into a small packet of weak gravity waves (Fig. 14a).

During the following 3-hour period, the simulation developed convective elements as the newly reorganized surface cold front progressed into a region of weak static stability over east-central Oklahoma. The vertical motion associated with these convective elements was accompanied by substantial moistening in the conditionally unstable lower troposphere (< 2.5 km AGL) (Figs. 14b, e). After 1100 UTC, the TB was able to encroach upon the wind shift, as its original forcing (the bore) rapidly decayed. At 1400 UTC, the wind shift, temperature and moisture features were again coincident and manifest as a surface cold front (Fig. 14d). By this time, the continued absence of negative Scorer parameter values along the cross-sectional domain ahead of the cold front illustrates that the prefrontal environment by that time was no longer able to support a bore by means of trapping the vertical propagation of wave energy. Thus, the analyzed segment of the cold front generated only small amplitude evanescent gravity waves as it moved across east-central Oklahoma (Fig. 14f).

Next, two supplementary series of cross-sections (along the pair of blue lines in Fig. 11) will be examined to show how the horizontal properties of the wave duct astride the primary cross-sections varied and evolved over time. The first of these supplemental cross-sections (series N in Fig. 11) captures the evolution of the wave duct to the north of the primary cross-

sections, while the second (series S in Fig. 11) describes such variations to the south of the primary cross-sections.

*b. Horizontal variations in the wave ducting mechanism*

Between 0500 and 1100 UTC, the bore / TB system moved southeastward to the north of the primary cross-sections, while to the south, the system moved predominately to the south (Fig. 11). The low-level stratification in cross-sections N1 and N2 (Figs. 15a, b) is similar to that shown in the primary cross-sections at both 0500 and 0800 UTC (Figs. 13a, d). A LLJ with a component opposing the movement of the bore / TB system is also present at both times within the stably-stratified surface layer (Figs. 15a, b). Also, the critical level rose from ~550 m to ~700 m AGL in the environment ahead of the system between 0500 and 0800 UTC (Figs. 15a, b). At these times, almost no component of the flow in the EML is oriented in the direction of motion of the bore / TB system (Figs. 15a, b). A region of negative Scorer parameter is located at ~700 m AGL at both times. However, since the vertical profile of the LLJ in the cross-sectional plane is nearly identical at both times, the more uniform distribution of the duct at 0800 UTC is likely a result of the increased stratification at the base of the EML (~400-1200 m AGL) (Figs. 15a, b). Finally, from 0800 to 1100 UTC, considerable weakening of the low-level stratification (surface to 2 km ASL) occurred along with a decay of the along cross-section wind component in the immediate pre-TB environment, resulting in the *absence* of a duct as indicated in the Scorer parameter field (Fig. 15c). To the southeast of the TB, the repositioning of the critical level from above the highly-stratified surface layer at 0800 UTC (Fig. 15b) to *within* the weakly-stratified surface layer at 1100 UTC (Fig. 15c), also favored the vertical propagation of wave energy (Lindzen and Tung 1976). In spite of a low-level wind profile favorable for

sustenance of the duct, erosion of the wave duct in the N series of cross-sections appears to result, as it did along the primary cross-sections, from a weakening of the low-level stratification.

To the south of the primary cross-sections, the presence of a highly stratified surface layer and EML aloft in the pre-bore environment at both 0500 and 0800 UTC (Figs. 15d, e) is similar to that shown in Figs. 13a and d. The component of the LLJ that opposes the movement of the bore / TB system in S1 and S2 is twice the magnitude (~17 m $s^{-1}$) of that shown in the N series as well as that shown in the primary cross-sections (compare Figs. 15a, b and Figs. 13a, b). Since the TB moved predominately southward along the S series of cross-sections (Fig. 11), the along cross-section component of the flow within the LLJ and EML (surface to ~1 km AGL) was much greater in cross-sections S1-S3 than cross-sections N1-N3 (compare Figs. 15a, d). This led to a deep layer of strong near-surface to mid-level flow counter to the movement of the bore / TB system (i.e. $U < 0$) which contributed to a deep layer of negative Scorer parameter (Figs. 15d-f). Unlike the flow in the N series and primary cross-sections, the magnitude of the ambient winds opposing the wave motion was ~8-9 m $s^{-1}$ within the EML, which was approximately the phase speed of the modeled solitary waves. Therefore, the layer at and above the base of the EML (~0.75-2 km AGL) acted as a critical layer (where $U = c_{bore}$ for a finite depth), promoting the reflection of wave energy below the layer at that time. By 1100 UTC, the wind structure in S3 (Fig. 15f) remained quite favorable for trapping vertical wave energy, while the surface stability weakened slightly from 0800 to 1100 UTC (similar to the primary and N series cross-sections) (Figs. 15e, f). Since both the primary and supplemental cross-sections possess a wind structure favorable for ducting in the pre-bore / TB environment, yet only S3 supported the presence of a duct at 1100 UTC, it can be concluded that the stronger background flow opposing the wave motion in the EML was favorable for wave trapping within the weakly-stratified surface layer to

the south of the primary cross-section between 0800 and 1100 UTC (compare Figs. 14c, 15c, f). The result was the development of an additional solitary wave packet (Region C Fig. 11) to the south of the primary bore (Region A Fig. 11) after 0800 UTC.

Finally, a series of calculations comparing characteristics of the observed and modeled cold front and evolving wave phenomena to values predicted from hydraulic theory are shown in the Appendix. These calculations provide additional supporting evidence that the wave phenomena examined here was a bore.

## 6. Discussion and Conclusions

Observations of bore signatures (pressure jumps) ahead of surface cold fronts have been discussed in the literature as far back as Tepper (1950). Since then, many studies have analyzed prefrontal features associated with a bore advancing ahead of a surface cold front (e.g. Haase and Smith 1984; Reeder and Smith 1992; Karyampudi et al. 1995; Reeder and Smith 1998; Deslandes et al. 1999; Koch and Clark 1999; Locatelli et al. 2002b). Analyses of the life cycles of such bores have most often focused on their roles in initiating convection and vertical moisture transport in the mid- and lower-troposphere (Karyampudi et al. 1995; Koch and Clark 1999; Locatelli et al. 2002b; Koch et al. 2008a) but not on their roles in promoting a separation between the wind shift and the thermodynamic properties of the parent cold front. In this paper, we have addressed the latter problem by identifying a feedback between the life cycle of the bore and the interaction of its associated wind shift with the parent cold front.

Schultz (2005) cited the generation of prefrontal bores and gravity waves as one possible mechanism for the formation of prefrontal troughs and wind shifts. In the present paper, it was

shown, through a detailed examination of surface and remotely-sensed observations as well as a high-resolution model simulation, that an undular bore associated with a cold frontal passage over the Southern Plains of the United States on 29 November 2006 was responsible for triggering a separation of the abrupt wind shift from the TB associated with a shallow, parent cold front. Not only was the bore linked to the development of this wind shift, but the subsequent decay of the bore ultimately led to the cold frontal passage observed at Okmulgee (Fig. 9), characterized by a merger of the previously disconnected wind shift and TB.

Initial observations at Larned suggest the movement of a cold front across west-central Kansas shortly before 0000 UTC 29 November 2006. Several hours later, a bore signature was evident in the SMOS observations at Lamont, Oklahoma; with vertical motion profiles from the MMCR and water vapor measurements from the Raman lidar at Lamont confirming the presence of an undular bore advancing out ahead of the surface TB. A surface pressure minimum was observed nearly an hour prior to the passage of the TB at Lamont. Just 34 minutes later, still prior to the passage of the TB, an abrupt wind shift, pressure jump, and slight surface warming were observed there. In the SMOS observations at Okmulgee, however, the pressure jump was observed to be coincident with a temperature and moisture drop, while a broad pressure minimum was recorded only a few minutes before passage of the surface cold front (Fig. 9).

The WRF simulation confirmed the existence of a wave packet and a wave duct sufficient for its support near 1 km AGL in the prefrontal environment over south-central Kansas and north-central Oklahoma. As the cold front moved into this environment around 0200 UTC, an undular bore formed along the boundary between a surface stable layer and a neutrally-stratified elevated mixed layer. A persistent LLJ was also present within the highly-stratified near-surface layer. Also, a wind shift developed at the leading edge of the bore and moved in tandem with the

head of the bore. Since the soliton and its associated surface wind shift moved faster than the surface TB, the features were systematically separated and the wind shift gradually evolved ahead of the TB. As the vertical circulation associated with the bore encroached upon the poleward edge of a reservoir of high $\theta_e$ air at the surface, this air was vertically lofted in the bore circulation. This increase in the depth of the moist surface layer occurred simultaneously with an increase in stable layer depth following the passage of the bore head as the entire system encroached upon both a progressively weaker surface stable layer to the SE and a persistent opposing LLJ. With the decrease in low-level stratification ahead of the bore, and the consequent repositioning of a critical level *within* the low-level stable layer, the wave duct weakened. This directly led to a weakening of the bore in the primary cross-sections. As the bore decayed, the TB was able to encroach upon the wind shift as its original forcing (the bore) rapidly disappeared. This circumstance led to a merger of the surface TB with the wind shift over northeastern Oklahoma.

An interesting aspect of the case examined here is the limited horizontal extent of the bore along the parent surface cold front (see Fig. 11). A number of prior studies have also noted this characteristic of undular bores (e.g. Haase and Smith 1989, Karyampudi et al. 1994), however none have fully explored the physical factors that act to limit their horizontal extent. We have presented an analysis of the horizontal extent of the present wave duct with a series of north (N) and south (S) secondary cross-sections. These cross-sections showed that the evolution of the duct to the north was similar to that observed in the primary cross-sections. The wave duct to the south persisted longer than its counterpart to the north because of stronger mid-level flow within the EML opposing the motion of the bore / TB system. The wind-profile curvature of the ambient flow opposing the wave motion and weak low-level stratification were

common characteristics in all cross-sections at 1100 UTC. The varying direction of movement of the TB along its length led to the different ambient wave duct characteristics shown in the three series of cross-sections (primary, N and S). The southward movement of the TB along S3 resulted in stronger opposing flow in the EML. Such a circumstance promoted the persistence of a critical layer that, in turn, supported the trapping of wave energy within the region of weak surface stratification ahead of the thermodynamic boundary.

Finally, the present study did not consider the sensible weather consequences of the merger of the bore-induced wind shift and the TB that occured after the decay of the bore. This issue and others are topics for future work. The availability of more than 10 years of high spatial- and temporal-resolution observational data from the ARM Program and Oklahoma Mesonet (Brock et al. 1995) over the Southern Plains, combined, as in this analysis, with fine resolution numerical simulations of selected events, will provide access to a large number of prefrontal bore cases through which study of the physical factors controlling the evolution of the prefrontal environment and its interaction with prefrontal bores will lend additional insight into these fascinating and perhaps characteristic features.

*Acknowledgements.* We express our appreciation to Pete Pokrandt for the data used in the synoptic overview and extensive GEMPAK support. All other data were obtained from the Atmospheric Radiation Measurement (ARM) Program sponsored by the U.S. Department of Energy, Office of Science, Office of Biological and Environmental Research, Climate and Environmental Sciences Division. Steve Koch (NOAA/ESRL) was very helpful in clarifying the definition of a bore and sounding analysis. Yvette Richardson (PSU), Chuck Doswell (CIMMS) and Greg Tripoli (UW-AOS) provided insight into the structure of wave ducts. D.D. Turner was

partially supported by grant DE-FG02-08ER64538 from the Department of Energy as part of the ARM program. D.C. Hartung and J. E. Martin were supported through Grant ATM-0806430 from the National Science Foundation. Rit Carbone, David Schultz and two other anonymous reviewers provided thorough comments that greatly enhanced the clarity and quality of this manuscript.

APPENDIX

According to hydraulic theory presented in Rottman and Simpson (1989), phase speed of a bore ($C_{\text{bore}}$) is a function of its depth ($d_{\text{b}}$), the depth of the inversion layer ($h_0$), and the shallow water gravity wave speed ($C_{\text{gw}}$) and can be found using the following equation (Koch and Clark 1999; Koch et al. 2008a):

$$C_{bore}/C_{gw} = [0.5(d_b/h_0)(1+d_b/h_0)]^{1/2} \qquad \text{(A1)}$$

Following the theory of Rottman and Simpson (1989), Koch et al. 2008 used the following set of equations to calculate the density current depth ($d_{\text{dc}}$), phase speed ($C_{\text{dc}}$), and the gravity wave speed ($C_{\text{gw}}$) of a bore:

$$d_{dc} = \frac{\theta_{vc}\Delta p}{\rho_w g[(p_c/p_w)\theta_{vw} - \theta_{vc}}\quad , \qquad \text{(A2)}$$

$$C_{dc} = Fr\left(\frac{\Delta p}{\rho_w}\right)^{1/2} \approx Fr\left(g d_{dc}\frac{\Delta\theta_v}{\theta_v}\right)^{1/2} \qquad \text{(A3)}$$

and

$$C_{gw} = \sqrt{g\Delta\theta_v(h_0/\theta_v)}\quad . \qquad \text{(A4)}$$

A caveat regarding the calculated hydraulic theory values is that, for this case, the cold front speed and depth are assumed to be those of a density current. Though not phenomenologically accurate, given the similarity between the modeled cold frontal speed (Table 1) and the density current speed predicted by hydraulic theory (Table 2), we consider this a reasonable approximation. A detailed explanation of variables used in these equations can be found in Section 6 of Koch et al. 2008 (p. 1394-1396). The method of Koch et al. 2008 has been applied to the WRF model output from the 29 November 2006 case with results shown in Table 2.

Rottman and Simpson (1989), Koch and Clark (1999) and Koch et al. (2008a) compared observations of a bore to calculated theoretical values. Calculations made from WRF model data associated with the bore and thermodynamic boundary passage at Lamont on 29 November 2006 are presented with values predicted from hydraulic theory to support the notion that the modeled phenomenon is a bore. Using the model input parameters shown in Table 1, a bore strength of 1.80 calculated from model data suggests that the WRF simulated bore was of similar strength to that observed at Lamont (Simpson 1997). Table 2 shows theoretical values of the modeled thermodynamic boundary speed and depth, bore depth and strength, and gravity wave speed based on the input parameter values of Table 1. The bore strength from hydraulic theory agrees very well with the bore strength estimated from observed and modeled values (1.62 vs. 1.77, 1.80) (Table 2). In general, the estimated bore strengths from observations, the WRF model, and hydraulic theory (1.62; 1.77; 1.80) agree well with one another and can be classified in the range in which laboratory experiments show that some turbulent mixing occurs behind the bore head (Rottman and Simpson 1989) (Tables 1, 2). It is important to note that any discrepancy between the bore strength predicted by hydraulic theory and that estimated from the WRF simulation is partially an artifact of the decrease in model grid spacing with height.

REFERENCES

Brock, F. V., K. C. Crawford, R. L. Elliott, G. W. Cuperus, S. J. Stadler, H. L. Johnson and M. D. Eilts. 1995. The Oklahoma Mesonet: A Technical Overview. *J. Atmos. Oceanic Technol.*, **12**, 5-19.

Carbone, R. E., J. W. Conway, N. A. Crook, and M. W. Moncrieff, 1990: The generation and propagation of nocturnal squall line. Part I: Observations and implications for mesoscale predictability. *Mon. Wea. Rev.,* **118,** 26-49.

Clark, R. H., R. K. Smith and D. G. Reid, 1981: The morning glory of the Gulf of Carpentaria: An atmospheric undular bore. *Mon. Wea. Rev.,* **109,** 1726-1750.

Clothiaux, E. E., K. P. Moran, B. E. Martner, T. P. Ackerman, G. G. Mace, T. Uttal, J. H. Maher, K. B. Widener, M. A. Miller, and D. J. Rodriguez, 1999: The Atmospheric Radiation Measurement program cloud radars: Operational modes. *J. Atmos. Oceanic Technol.,* **16,** 819-827.

Crook, N. A., 1986: The effect of ambient stratification and moisture on the motion of atmospheric undular bores. *J. Atmos. Sci.,* **43,** 171-181.

_____, 1988: Trapping of low-level internal gravity waves. *J. Atmos. Sci.,* **45,** 1533-1541.

Deslandes, R., M. J. Reeder, and G. A Mills, 1999: Synoptic analyses of a subtropical cold front observed during the 1991 Central Australian Fronts Experiment. *Aust. Meteor., Mag*., **48**, 87-110.

Dudhia, J., 1989: Numerical study of convection observed during the winter monsoon experiment using a mesoscale two dimensional model. *J. Atmos. Sci.,* **46,** 3077–3107.

Ferrare, R.A., D.D. Turner, M. Clayton, B. Schmid, J. Redemann, D. Covert, R. Elleman, J. Ogren, E. Andrews, J.E.M. Goldsmith, and H. Johsson, 2006: Evaluation of daytime measurements of aerosols and water vapor made by an operational Raman lidar over the Southern Great Plains. *J. Geophys. Res.,* **111,** D05S08, doi:10.1029/2005JD005836.

Goldsmith, J. E. M., F. H. Blair, S. E. Bisson, and D. D. Turner, 1998: Turn-key Raman lidar for profiling atmospheric water vapor, clouds, and aerosols. *Appl. Opt.,* **37,** 4979-4990.

Goler, R. A., 2009: Eastward propagating undular bores over Cape York Peninsula. *Mon. Wea. Rev.,* **137,** 2632-2645.

_____ and M. J. Reeder, 2004: The generation of the morning glory. *J. Atmos. Sci.,* **61,** 1360-1376.

_____, _____, R. K. Smith, H. Richter, S. Arnup, T. Keenan, P. May, and J. Hacker, 2006: Low-level convergence lines over northeastern Australia. Part I: The north Australian cloud line. *Mon. Wea. Rev.,* **134,** 3092-3108.

Haase, S. P. and R. K. Smith, 1984: Morning glory wave clouds in Oklahoma: A case study. *Mon. Wea. Rev.,* **112,** 2078-2089.

_____ and _____, 1989: The numerical simulation of atmospheric gravity currents. Part II: Environments with stable layers. *Geophys. Astrophys. Fluid Dyn.,* **46,** 35-51.

Haertel, P. T., R. H. Johnson, and S. N. Tulich, 2001: Some simple simulations of thunderstorm outflows. *J. Atmos. Sci.,* **58,** 504-516.

Hutchinson, T. A., and H. B. Bluestein, 1998: Prefrontal wind-shift lines in the plains of the United States. *Mon. Wea. Rev.,* **126,** 141-166.

Karyampudi, V. M., S. E. Koch, C. Chen, J. W. Rottman, and M. L. Kaplan, 1995: The influence of the Rocky Mountains on the 13-14 April 1986 severe weather outbreak. Part II: Evolution of a prefrontal bore and its role in triggering a squall line. *Mon. Wea. Rev.,* **123,** 1423-1446.

Koch, S. E., P. B. Dorian, R. Ferrare, S. H. Melfi, W. C. Skillman, and D. Whiteman, 1991: Structure of an internal bore and dissipating gravity current as revealed by Raman lidar. *Mon. Wea. Rev.,* **119,** 857-887.

_____ and W. L. Clark, 1999: A nonclassical cold front observed during COPS-91: Frontal structure and the process of severe storm initiation. *J. Atmos. Sci.,* **56,** 2862-2890.

_____ and C. O'Handley, 1997: Operational forecasting and detection of mesoscale gravity waves. *Wea. and Forecasting,* **12,** 253-281.

_____, W. F. Feltz, F. Fabry, M. Pagowski, B. Geerts, K. M. Bedka, D. O. Miller, and J. W. Wilson, 2008a: Turbulent mixing processes in atmospheric bores and solitary waves deduced from profiling systems and numerical simulation. *Mon. Wea. Rev*., **136,** 1373-1400.

_____, C. Flamant, J. M. Wilson, B. M. Gentry, and B. D. Jamison, 2008b: An atmospheric soliton observed with Doppler radar, differential absorption lidar, and molecular Doppler lidar. *Journ. Atmos. Oceanic Tech.,* **25,** 1267-1287.

Kollias, P., E. E. Clothiaux, M. A. Miller, E. P. Luke, K. L. Johnson, K. P. Moran, K. B. Widener, and B. A. Albrecht, 2007: The Atmospheric Radiation Measurement program cloud profiling radars: Second-generation sampling strategies, processing, and cloud data products. *J. Atmos. Oceanic Technol.,* **24,** 1199-1214.

Lindzen, R. S. and K. K. Tung, 1976: Banded convective activity and ducted gravity waves. *Mon. Wea. Rev.,* **104,** 1602-1617.

Locatelli, J. D., M. T. Stoelinga, P. V. Hobbs, and J. Johnson 1998: Structure and evolution of an undular bore on the High Plains and its effects on migrating birds. *Bull. Amer. Meteor. Soc.,* **79**, 1043-1060.

_____, _____, and _____, 2002b: A new look at the super outbreak of tornadoes on 3-4 April 1974. *Mon. Wea. Rev.,* **130,** 1633-1651.

Mahapatra, P. R., R. J. Doviak, and D. S. Zrnic 1991: Multisensor observation of an atmospheric undular bore. *Bull. Amer. Meteor. Soc.,* **72**, 1468-1480.

Martin, J. E., J. D. Locatelli, P. V. Hobbs, P-Y. Wang and J. A. Castle: Structure and evolution of winter cyclones in the central United States and their effects on the distribution of precipitation. Part I: A synoptic scale rainband associated with a dryline and lee trough. *Mon. Wea. Rev.,* **123,** 241-264.

Mellor, G. L., and T. Yamada, 1982: Development of a turbulence closure model for geophysical fluid problems. *Rev. Geophys. Space Phys.,* **20,** 851–875.

Menhofer, A., R. K. Smith, M. J. Reeder and D. R. Christie, 1997: The bore-like character of three morning glories observed during the Central Australian Fronts Experiment. *Aust. Meteor. Mag.,* **46,** 277-285.

_____, _____, _____ and _____, 1997: "Morning-Glory" disturbances and the environment in

which they propagate. *J. Atmos. Sci.,* **54,** 1712-1725.

Mlawer, E. J., S. J. Taubman, P. D. Brown, M. J. Iacono, and S. A. Clough, 1997: Radiative transfer for inhomogeneous atmospheres: RRTM, a validated correlated-k model for the longwave. *J. Geophys. Res.,* **102(D14),** 16,663-16,682.

Moran, K. P., B. E. Martner, M. J. Post, R. A. Kropfli, D. C. Welsh, and K. B. Widener, 1998: An unattended cloud-profiling radar for use in climate research. *Bull. Amer. Meteor. Soc.,* **79,** 321-342.

Newsom, R. K., D. D. Turner, B. Mielke, M. Clayton, R. Ferrare and C. Siveraman 2009: Simultaneous analog and photon counting detection for Raman lidar. *Appl. Opt.,* **48,** 3903-3914.

Noonan, J. A. and R. K. Smith, 1986: Sea-breeze circulations over Cape York Peninsula and the generation of Gulf of Carpentaria cloud line disturbances. *J. Atmos. Sci.,* **43,** 1679-1693.

Reeder, M. J., and R. K. Smith, 1992: Australian spring and summer cold fronts. *Aust. Meteor. Mag*., **41**, 101-124.

_____ and _____, 1998: *Mesoscale Meteorology, Meteorology of the Southern Hemisphere*, Eds. D. Vincent and D. J. Karoly, American Meteorological Society, p. 201-241.

Rottman, J. W. and J. E. Simpson, 1989: The formation of internal bores in the atmosphere: A laboratory model. *Quart. J. Roy. Meteor. Soc.,* **115,** 941-963.

Sakai, T., T. Nagai, T. Matsumura, M. Nakazato, and M. Sasaoka, 2005: Vertical structure of a nonprecipitating cold frontal head as revealed by Raman lidar and wind profiler observations. *J. Meteor. Soc. Japan,* **83,** 293-304.

Sanders, F., 1999: A proposed method of surface map analysis. *Mon. Wea. Rev.,* **127,** 945-955.

Schultz, D. M., 2004: Cold fronts with and without prefrontal wind shifts in the central United States. *Mon. Wea. Rev.,* **132,** 2040-2053.

_____, 2005: A review of cold fronts with prefrontal troughs and wind shifts. *Mon. Wea. Rev.,* **133,** 2449-2472.

Scorer, R., 1949: Theory of waves in the lee of mountains. *Quart. J. Roy. Meteor. Soc.,* **75,** 41-56.

Simpson, J. E., 1997: *Gravity Currents: In the Environment and the Laboratory 2nd Edition*. Cambridge University Press, 244p.

Smith, R. K. 1988: Travelling waves and bores in the lower atmosphere: The 'Morning Glory' and related phenomena. *Earth-Sci. Rev.,* **25,** 267-290.

_____ and B. R. Morton, 1984: An observational study of northeasterly “morning glory” wind surges. *Aust. Meteor. Mag.,* **32,** 155-175.

_____ and M. A. Page, 1985: Morning glory wind surges and the Gulf of Carpentaria cloud line of 25-26 October 1984. *Aust. Meteor. Mag.,* **33,** 185-194.

Tepper, M., 1950: A proposed mechanism of squall lines: The pressure jump line. *J. Meteor.,* **7,** 21-29.

Thompson, G., P. R. Field, W. D. Hall, and R. M. Rasmussen, 2006: A new bulk microphysical parameterization for WRF & MM5. Preprints, *Seventh Weather Research and Forecasting User’s Workshop,* Boulder, CO, NCAR, 5.3 [Available online at http://www.mmm.ucar.edu/wrf/users/workshops/ WS2006/WorkshopPapers.htm.]

Turner, D. D., and J. E. M. Goldsmith, 1999: Twenty-four-hour Raman lidar water vapor measurements during the Atmospheric Radiation Measurement Program's 1996 and 1997 water vapor intensive observation periods. *J. Atmos. Oceanic Technol.,* **16,** 1062-1076.

_____, W. F. Feltz, and R. A. Ferrare, 2000: Continuous water vapor profiles from operational ground-based active and passive remote sensors. *Bull. Amer. Meteor. Soc.,* **81,** 1301-1317.

Wakimoto, R. M., 1982: The life cycle of thunderstorm gust fronts as viewed with Doppler radar

and rawinsonde data. *Mon. Wea. Rev.,* **110,** 1060-1082.

Wood, I. R. and J. E. Simpson, 1984: Jumps in layered miscible fluids. *J. Fluid Mech.,* **104,** 329-342.

TABLE CAPTIONS

Table 1: Input parameter values, estimated bore strength and critical level at Lamont from observed and WRF model values. Data sources are displayed under "Data source or method of calculation". (Adapted from Koch et al. 2008a)

Table 2: Bore phase speed and depth predicted from hydraulic theory using WRF model input parameter values from Table 1. (Adapted from Koch et al. 2008a)

FIGURE CAPTIONS

Fig. 1: Conceptual model of a soliton with an undular bore generated by a cold front adapted from Fig. 1a of Locatelli et al. (1998) and Fig. 13.4 from Simpson (1997). Arrows indicate the direction of flow at various locations. Largest black arrow depicts movement of the bore generated by the intrusion of the cold front into the stable layer.

Fig. 2: Geographic representation of domain 1 and domain 2 of the WRF model simulation. Solid lines in domain 2 indicate cross-sections examined from (i) Hill City, Kansas to (ii) Zenith, Kansas, (ii) Zenith to (iii) Red Rock, Oklahoma, and (iv) Lamont, Oklahoma to (v) Stidham, Oklahoma. Dashed lines show the approximate location of the surface thermodynamic boundary at the indicated times. Stars indicate the location of the three ARM surface observation sites used in this analysis including: (a) Larned, Kansas, (b) Lamont, Oklahoma, and (c) Okmulgee, Oklahoma. Lamont is also the ARM central facility for the Raman lidar and MMCR.

Fig 3: Eta model analyses valid at 0000 UTC on 29 November 2006 of (a) sea-level pressure contoured every 4 hPa (thick black) with 950 hPa potential temperature contoured every 4 K (dashed lines), (b) 850 hPa geopotential height contoured every 60 meters (thick black) with temperature contoured every 4 °C (dashed lines) and (c) 500 hPa geopotential height contoured every 60 meters (thick black) with temperature contoured every 4 °C (dashed lines) and absolute vorticity shaded every $5 \times 10^{-5}$ $s^{-1}$ beginning at $20 \times 10^{-5}$ $s^{-1}$. Bold dashed line in (a) represents the position of the surface drytrough (see text for explanation).

Fig. 4: Same as Figure 3 except valid at 1200 UTC 29 November 2006.

Fig. 5: Same as Figure 3 except valid at 0000 UTC 30 November 2006.

Fig 6: Surface observations from 2200 UTC 28 November 2006 to 0200 UTC 29 November 2006 from the Larned, Kansas SMOS station. Displayed variables include: (a) 2 meter temperature in degrees Celsius, (b) 2 meter water vapor mixing ratio in g $kg^{-1}$, (c) 2 meter cardinal wind direction, and (d) 1 meter barometric pressure in hPa. The dashed grey line marks the time of the surface cold frontal passage at the station.

Fig 7: Surface observations from 0700 to 1100 UTC 29 November 2006 from the Lamont, Oklahoma SMOS station. Displayed variables are the same as in Figure 6. The dashed grey line marks the time of the thermodynamic boundary passage, the dashed black line indicates the time of the bore passage (commencement of wind shift and pressure jump) and the solid grey line marks the observed time of the lowest recorded barometric pressure at the station.

Fig 8: Time-height cross-sections of (a) vertical velocity derived from the MMCR and (b) water vapor mixing ratio derived from the Raman lidar from 0800 to 1000 UTC 29 November 2006 at Lamont, Oklahoma. Black arrow indicates time of passage of first undulation and grey arrow notes time of passage of thermodynamic boundary. Raman lidar water vapor data have been processed to yield a 10-sec, 75-meter resolution.

Fig 9: Same as Figure 7, except valid from 1500 to 1900 UTC 29 November 2006 at the Okmulgee, OK SMOS station.

Fig. 10: Sounding taken from the Lamont, Oklahoma, ARM site at 0532 UTC 29 November 2006. The bold black line is the vertical temperature profile and the bold blue line is the vertical dewpoint temperature profile. Wind speed and direction are indicated by the wind barbs to the right using the following convention for speed: half-barb, 2.5 m $s^{-1}$; full-barb, 5 m $s^{-1}$; flag, 25 m $s^{-1}$.

Fig. 11: Shaded vertical velocity (m $s^{-1}$) at 1 km ASL from Domain 2 of WRF model simulation valid at (a) 0030 UTC, (b) 0500 UTC, (c) 0800 UTC and (d) 1100 UTC 29 November 2006. Labeled regions (A, B, C) are discussed in the text. Bold black line is the smoothed surface 290 K isotherm indicative of the leading edge of the surface thermodynamic boundary. Grey lines show cross-sections from Figure 2 and are discussed in Figures 12-14. Wind barbs represent horizontal wind speed and direction at 0.5 km ASL with one full barb corresponding to 5.0 m $s^{-1}$. Light blue lines mark the location of the north (N) and south (S) series of cross-sections shown in Figure 15.

Fig 12: Vertical cross-section of WRF model output from Albert, KS to Red Rock, OK (along line *i-ii* in Fig. 11). Left hand column is valid at 0030 UTC and right hand column is valid at 0200 UTC 29 November. Panels (a) and (d) show potential temperature (solid black) contoured every 2 K, along cross-section horizontal wind vectors and vertical motion shaded every 0.35 m $s^{-1}$ according to scale at right. Bold black line is the 290 K isentrope. Panels (b) and (e) show mixing ratio in g $kg^{-1}$ shaded every 0.25 g $kg^{-1}$ and equivalent potential temperature (white) contoured every 2 K. Panels (c) and (f) show the Scorer parameter shaded every $0.3 \times 10^{-6}$ $m^{-2}$

with all values less than $-3x10^{-6}$ saturated with solid purple and all values greater than $10^{-5}$ saturated in pink and potential temperature contoured in solid black from 288 K to 298 K. Horizontal black arrows indicate direction and magnitude of along cross-section wind component with longest arrows corresponding to a 12 m $s^{-1}$ wind speed. Blue arrows indicate position of surface thermodynamic boundary (290 K isentrope) and red arrows indicate position of surface wind shift. Bold black dashed lines indicate the critical level ahead of the bore / TB system. Vertically-oriented black arrows point to region characterized by a low-level stable layer and grey star indicates location of Larned, Kansas in the cross-section.

Fig 13: WRF simulation output along cross-section *ii*-*iii* in Figure 11. Data shown is the same as Figure 12, but left column displays data valid at 0500 UTC and right column shows data from 0800 UTC 29 November. Longest along cross-section arrows correspond to a 17 m $s^{-1}$ wind speed. Grey star indicates location of Lamont, Oklahoma in the cross-section.

Fig. 14: WRF simulation output along cross-section *iv*-*v* in Figure 11. Data shown is the same as Figure 13, but left column displays data valid at 1100 UTC and right column shows data from 1400 UTC 29 November. Longest along cross-section arrows correspond to a 13 m $s^{-1}$ wind speed. Grey star indicates location of Okmulgee, Oklahoma in the cross-section.

Fig. 15: Vertical cross-sections of WRF model output from N series (left column) and S series (right column) cross-sections in Figure 11. Panels (a)-(c) are taken along N1, N2 and N3 in Fig. 11 respectively. Likewise, panels (d)-(f) are taken along S1, S2 and S3 in Fig. 11 respectively. Panels (a) and (d) (top row) are valid at 0500 UTC, panels (b) and (e) (middle row) are valid at

0800 UTC and panels (c) and (f) (bottom row) are valid at 1100 UTC 29 November 2006. All panels show the Scorer parameter shaded as in Figs. 12-14. Potential temperature is contoured in white with the 290 K isentrope (indicating the position of the surface thermodynamic boundary) contoured in black. Horizontal black arrows indicate direction and magnitude of along cross-section wind component with longest arrows corresponding to 12 m $s^{-1}$ in the left column and 17 m $s^{-1}$ in the right column. Bold black dashed lines indicate the critical level ahead of the bore / TB system. Bold dashed white lines indicate the base of a layer where $U = c_{bore}$ (critical layer).

TABLE 1

Table 1: Input parameter values, estimated bore strength and critical level at Lamont from observed and WRF model values. Data sources are displayed under "Data source or method of calculation". (Adapted from Koch et al. 2008a)

| Symbol | Parameter | Units | Obs. | WRF | Data source or method of calculation |
|---|---|---|---|---|---|
| $H$ | Tropopause height | km | 12.50 | 15.70 | 0532 UTC Lamont sounding (Fig. 10) / WRF Lamont sounding 0800 UTC |
| $d_b$ | Bore depth | km | 0.70 | 0.90 | Estimate from MMCR (Fig. 8a) / WRF cross-section analysis 0800 UTC (Fig. 13d) |
| $h_0$ | Inversion depth | km | 0.43 | 0.50 | 0532 UTC Lamont sounding (Fig. 10) / WRF cross-section analysis 0800 UTC (Fig. 13d) |
| $\Delta\theta$ | Inversion strength | K | 5.80 | 3.40 | 0532 UTC Lamont sounding (Fig. 10) / WRF Lamont sounding 0800 UTC |
| $\Delta\theta_{dc}$ | Cold front cooling | K | 4.50 | 4.00 | Temperature drop at source of pressure jump (Fig. 7) / WRF Lamont sounding 0800 UTC and 1000 UTC |
| $C_{dc}$ | Cold front speed | m $s^{-1}$ | 6.30 | 8.20 | Analysis of SMOS observations from Lamont and Okmulgee (Figs. 7, 9) / WRF cross-section analysis from 0800-1100 UTC (Figs. 13d, 14a) |
| $U$ | Mean head wind | m $s^{-1}$ | 15.60 | 13.10 | 0532 UTC Lamont sounding (Fig. 10) using $C_{dc}$ value / WRF cross-section analysis from 0800 UTC (Fig. 13d) using model $C_{dc}$ value |
| $d_b/h_0$ | Bore strength | ----- | 1.62 | 1.80 | Simple Ratio |
| ---------- | ---------- | ----- | ---------- | ---------- | ---------- |
| $U_n = C_{dc}$ | Critical Level | km | 0.61 | 0.55 | Estimate from 0532 UTC Lamont sounding (Fig. 10), $C_{dc}$ and fixed cold front motion vector of 320° / model estimate from 0800 UTC cross-section (Fig. 13f) |
| $\Delta p$ | Pressure jump | hPa | 1.00 | ------ | Magnitude of pressure jump in cold front vicinity |
| $\lambda$ | Horizontal wavelength | km | 9.60 | 10.00 | Product of MMCR analysis (Fig. 8a) / WRF cross-section 0800 UTC (Fig. 13d) |

TABLE 2

Table 2: Bore phase speed and depth predicted from hydraulic theory using WRF model input parameter values from Table 1. (Adapted from Koch et al. 2008a)

| Symbol | Parameter | Units | Value | Data source or method of calculation |
|---|---|---|---|---|
| $d_{dc}$ | Cold front depth | km | 0.46 | Equation 3 (Appendix A) |
| $d_{dc} / h_0$ | Normalized cold front depth | --- | 1.53 | Simple Ratio |
| $C_{dc}$ | Cold front speed | m $s^{-1}$ | 8.78 | Equation 4 (Appendix A) |
| $C_{gw}$ | Gravity wave speed | m $s^{-1}$ | 9.54 | Equation 5 (Appendix A) |
| $C_{dc}/C_{gw}$ | Froude number | --- | 0.92 | Simple Ratio |
| $d_b/h_0$ | Predicted bore strength | --- | 1.77 | Koch and Clark (1999, Table 3) / Rottman and Simpson (1989) |
| $d_b$ | Predicted bore depth | km | 0.53 | Product of predicted $d_b/h_0$ and modeled $h_0$ |

FIGURE 1

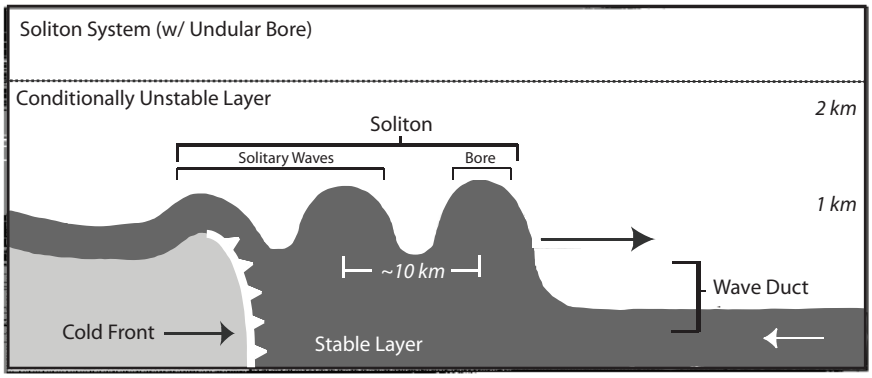


Fig. 1: Conceptual model of a soliton with an undular bore generated by a cold front adapted from Fig. 1a of Locatelli et al. (1998) and Fig. 13.4 from Simpson (1997). Arrows indicate the direction of flow at various locations. Largest black arrow depicts movement of the bore generated by the intrusion of the cold front into the stable layer.

FIGURE 2

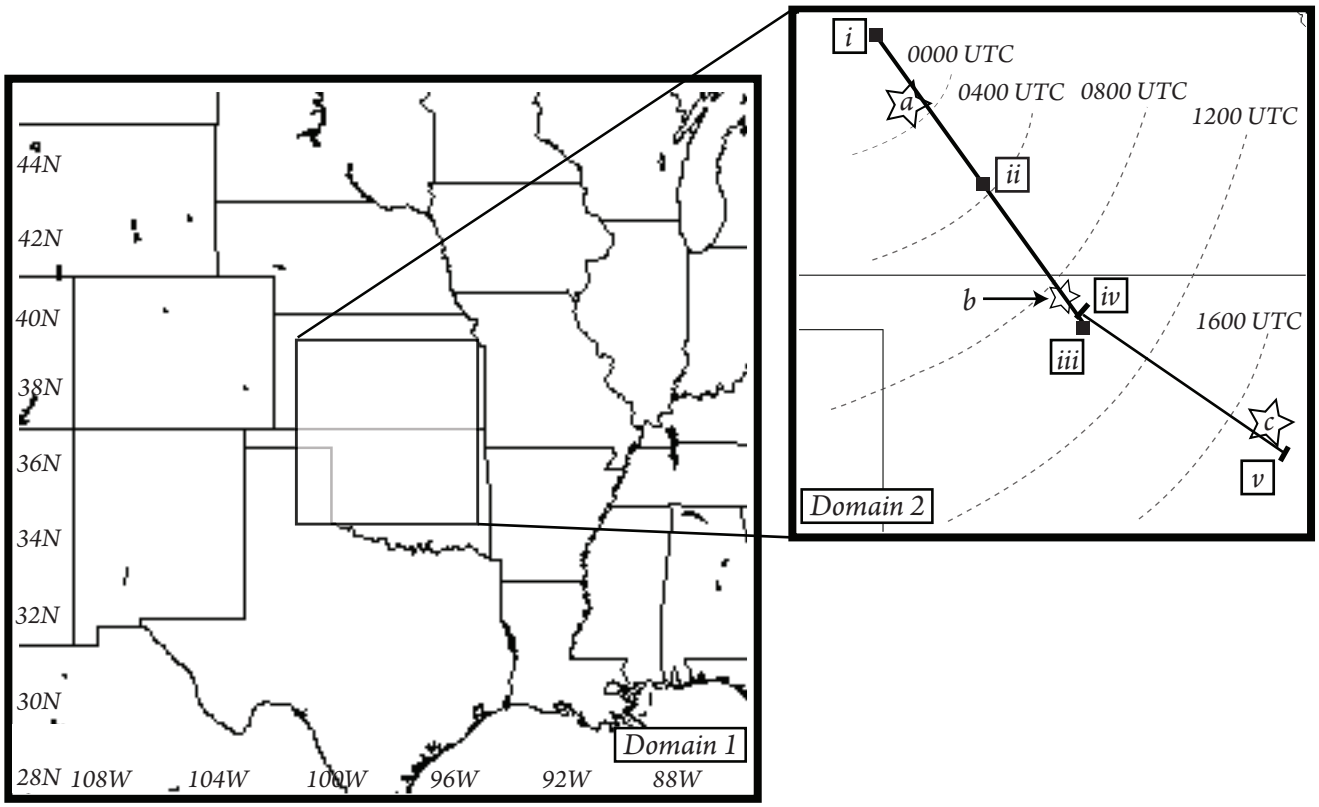


Fig. 2: Geographic representation of domain 1 and domain 2 of the WRF model simulation. Solid lines in domain 2 indicate cross-sections examined from (i) Hill City, Kansas to (ii) Zenith, Kansas, (ii) Zenith to (iii) Red Rock, Oklahoma, and (iv) Lamont, Oklahoma to (v) Stidham, Oklahoma. Dashed lines show the approximate location of the surface thermodynamic boundary at the indicated times. Stars indicate the location of the three ARM surface observation sites used in this analysis including: (a) Larned, Kansas, (b) Lamont, Oklahoma, and (c) Okmulgee, Oklahoma. Lamont is also the ARM central facility for the Raman lidar and MMCR.

FIGURE 3

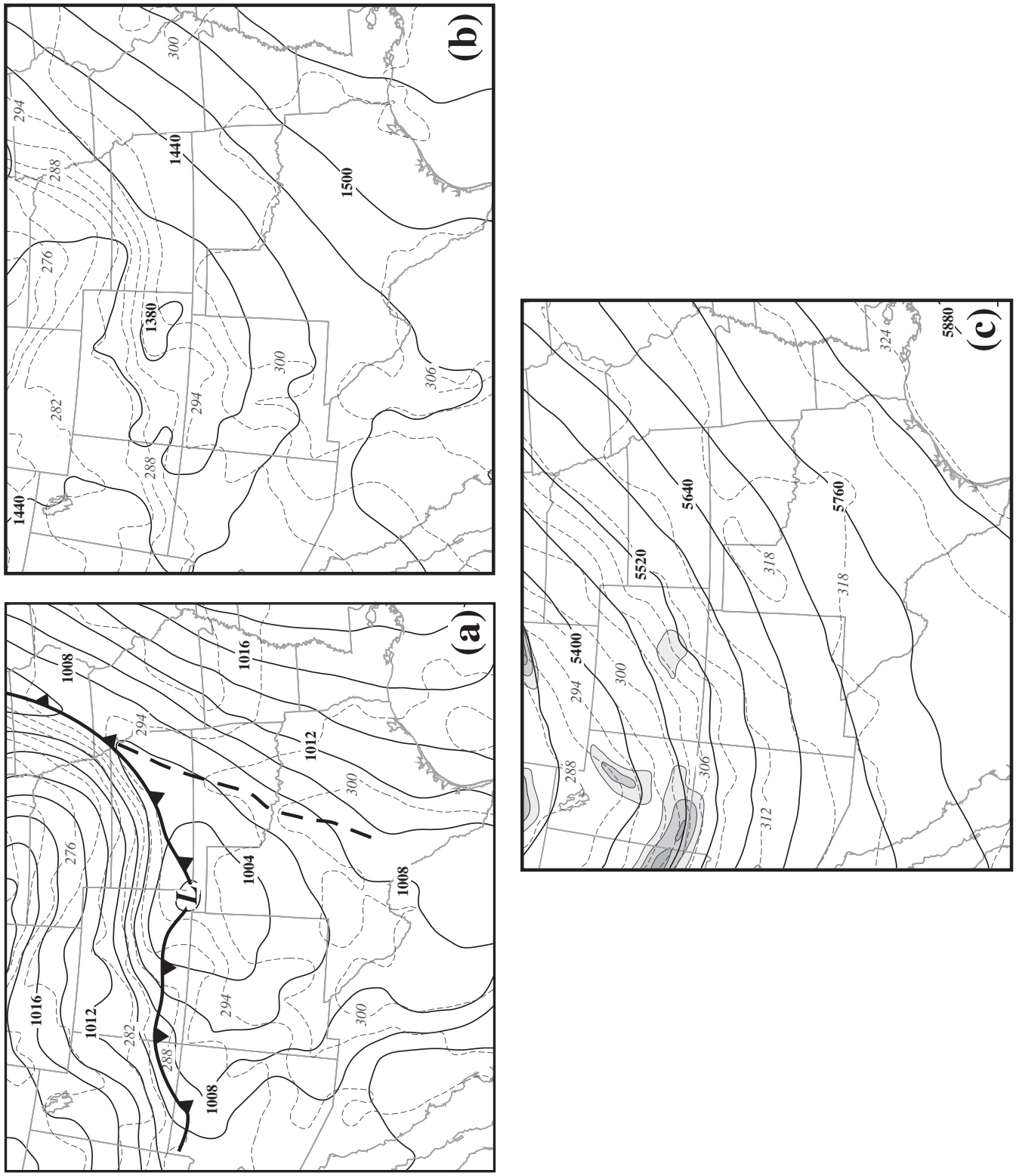


Fig 3: Eta model analyses valid at 0000 UTC on 29 November 2006 of (a) sea-level pressure contoured every 4 hPa (thick black) with 950 hPa potential temperature contoured every 4 K (dashed lines), (b) 850 hPa geopotential height contoured every 60 meters (thick black) with temperature contoured every 4 °C (dashed lines) and (c) 500 hPa geopotential height contoured every 60 meters (thick black) with temperature contoured every 4 °C (dashed lines) and absolute vorticity shaded every $5 \times 10^{-5}$ $s^{-1}$ beginning at $20 \times 10^{-5}$ $s^{-1}$. Bold dashed line in (a) represents the position of the surface drytrough (see text for explanation).

FIGURE 4

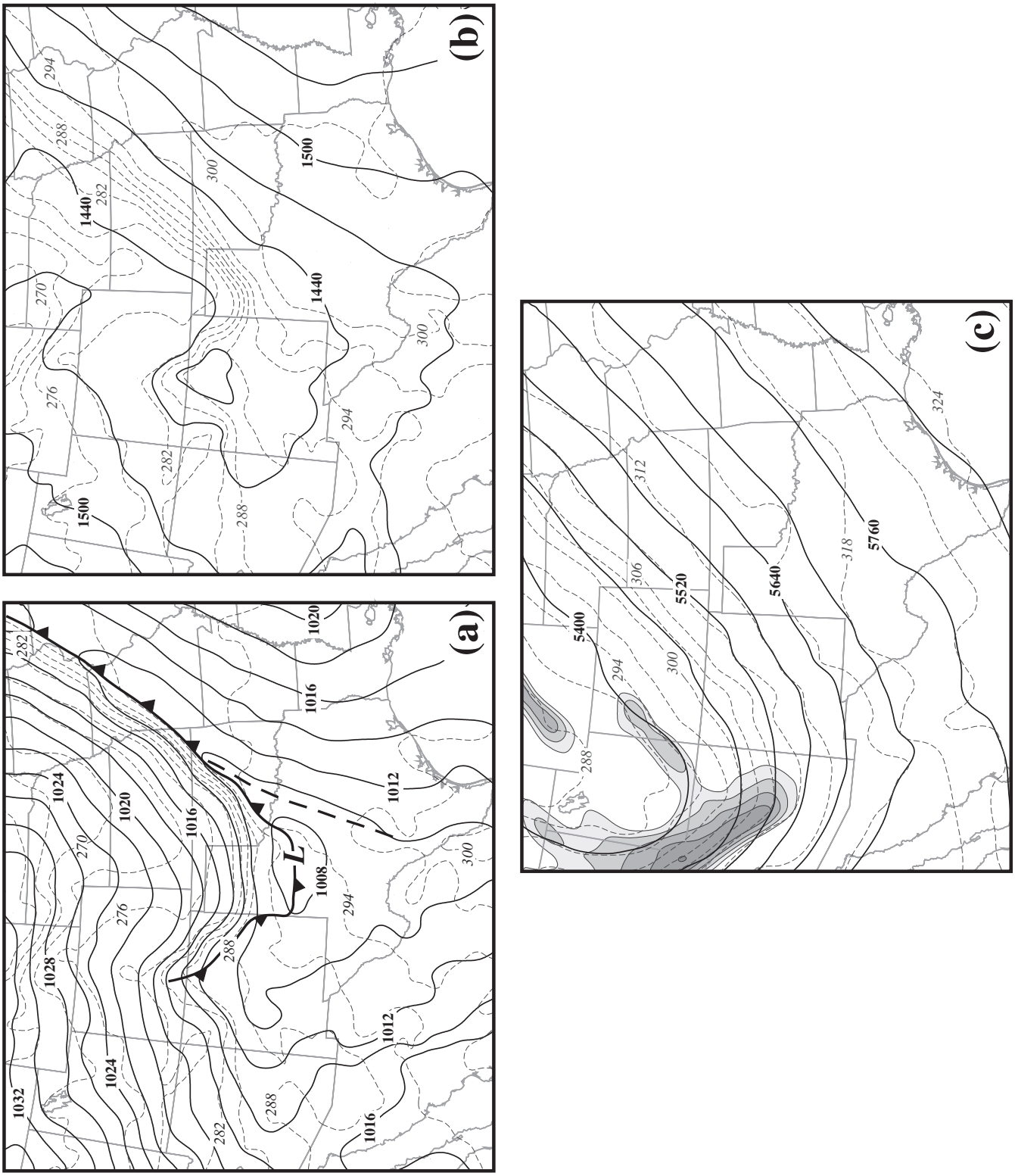


Fig. 4: Same as Figure 3 except valid at 1200 UTC 29 November 2006.

FIGURE 5

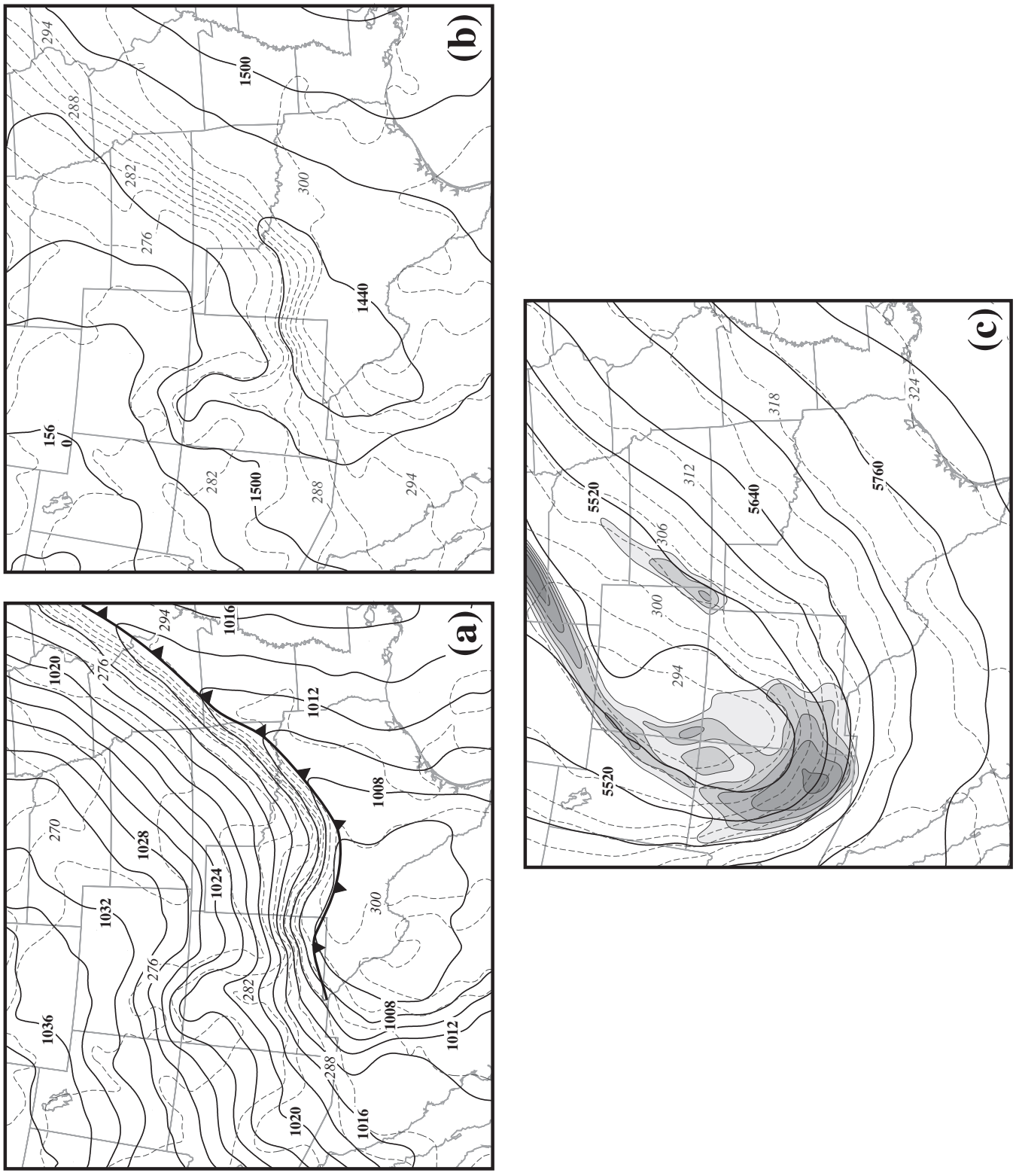


Fig. 5: Same as Figure 3 except valid at 0000 UTC 30 November 2006.

FIGURE 6

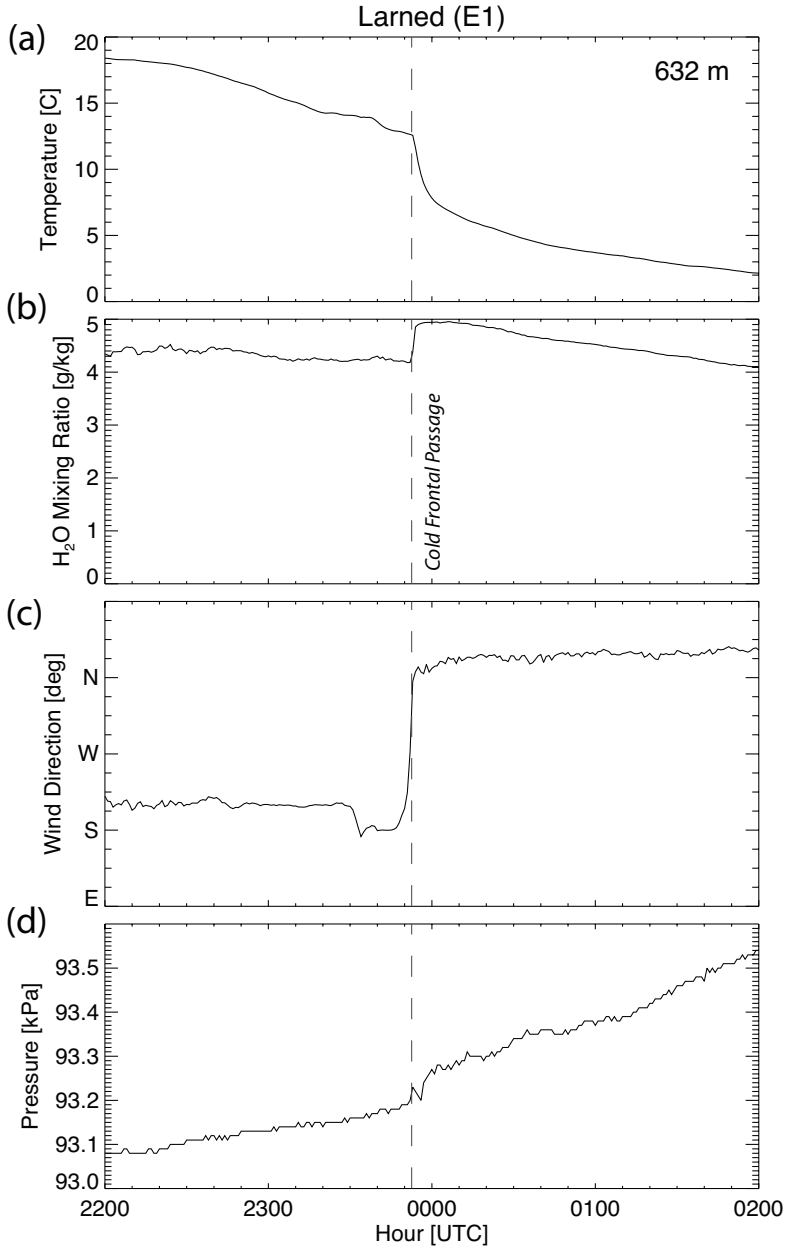


Fig 6: Surface observations from 2200 UTC 28 November 2006 to 0200 UTC 29 November 2006 from the Larned, Kansas SMOS station. Displayed variables include: (a) 2 meter temperature in degrees Celsius, (b) 2 meter water vapor mixing ratio in g $kg^{-1}$, (c) 2 meter cardinal wind direction, and (d) 1 meter barometric pressure in hPa. The dashed grey line marks the time of the surface cold frontal passage at the station.

FIGURE 7

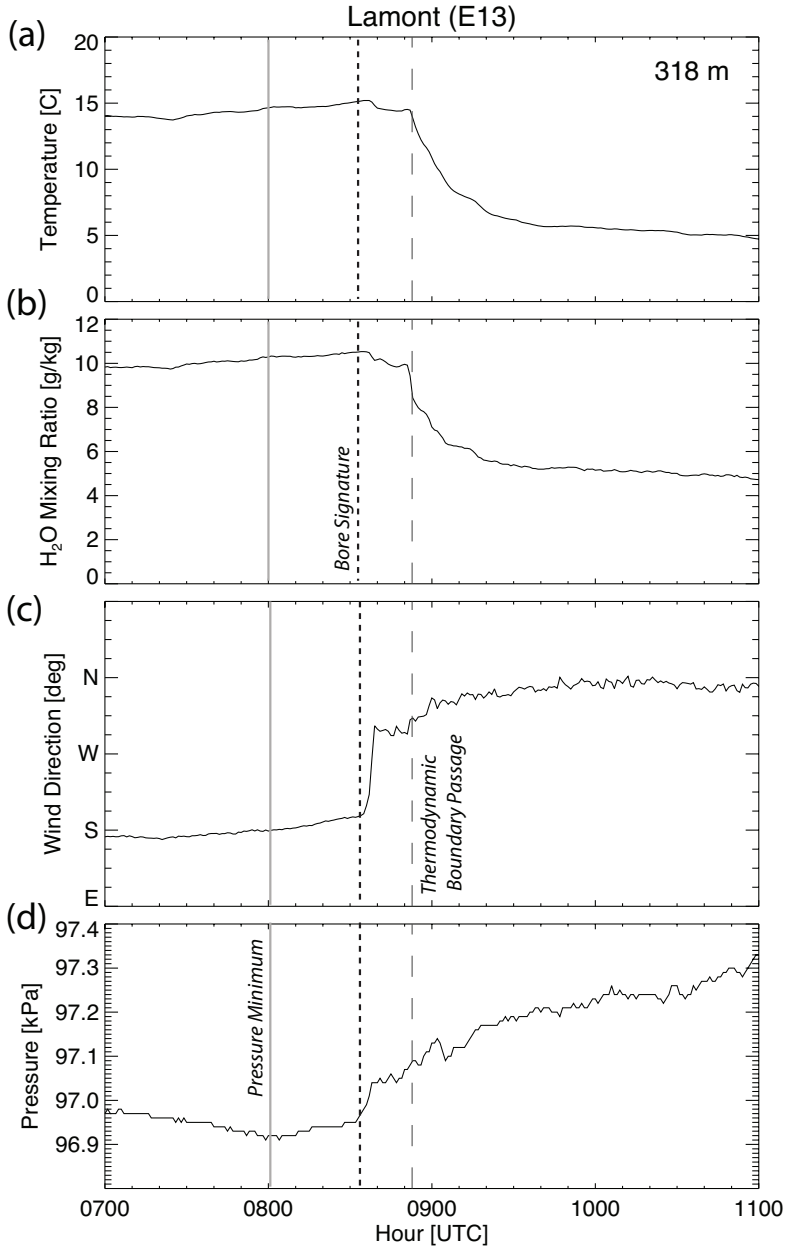


Fig 7: Surface observations from 0700 to 1100 UTC 29 November 2006 from the Lamont, Oklahoma SMOS station. Displayed variables are the same as Figure 6. The dashed grey line marks the time of the thermodynamic boundary passage, the dashed black line indicates the time of the bore passage (commencement of wind shift and pressure jump) and the solid grey line marks the observed time of the lowest recorded barometric pressure at the station.

FIGURE 8:

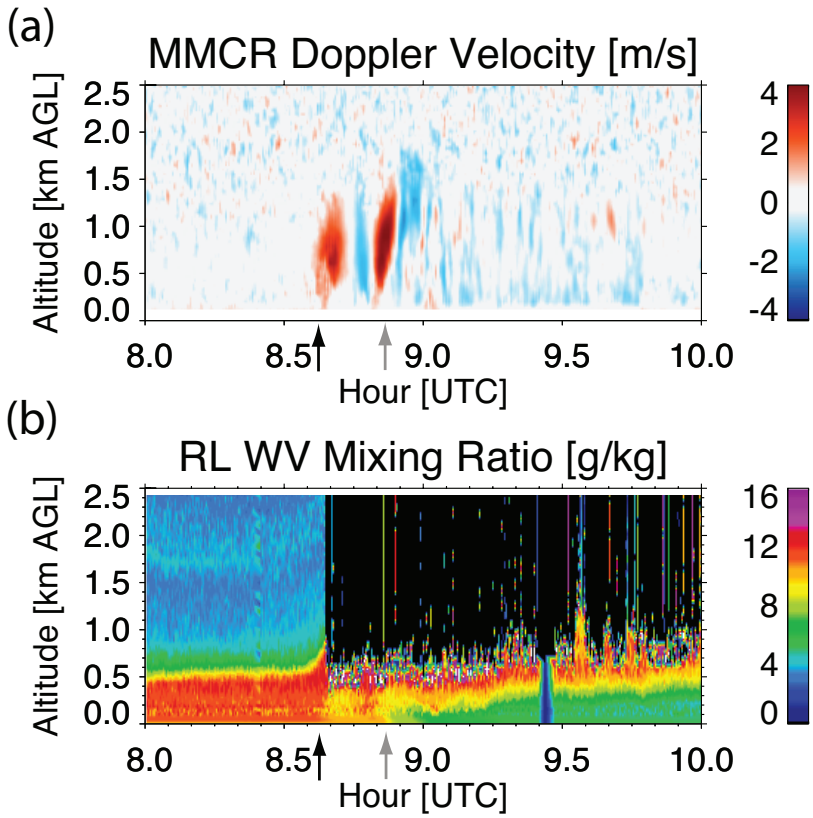


Fig 8: Time-height cross-sections of (a) vertical velocity derived from the MMCR and (b) water vapor mixing ratio derived from the Raman lidar from 0800 to 1000 UTC 29 November 2006 at Lamont, Oklahoma. Black arrow indicates time of passage of first undulation and grey arrow notes time of passage of thermodynamic boundary. Raman lidar water vapor data have been processed to yield a 10-sec, 75-meter resolution.

FIGURE 9

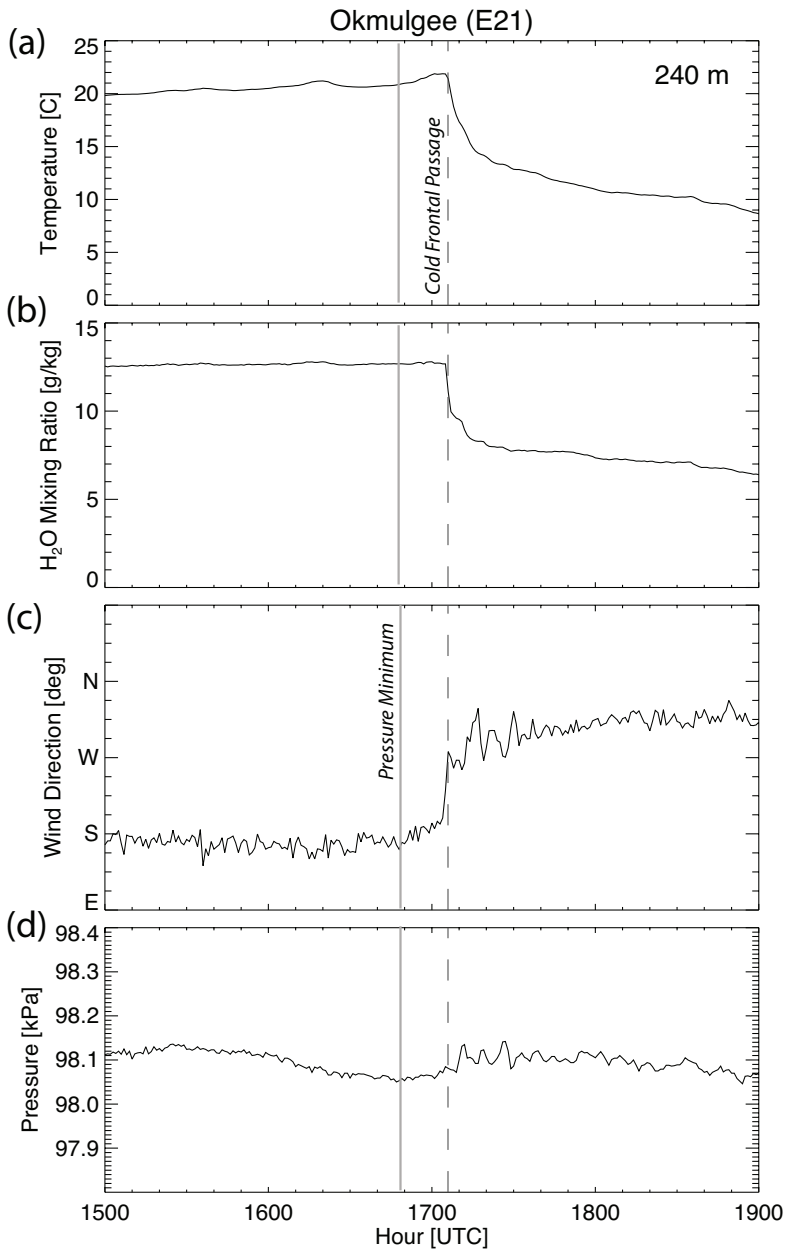


Fig 9: Same as Figure 7, except valid from 1500 to 1900 UTC 29 November 2006 at the Okmulgee, OK SMOS stations.

FIGURE 10

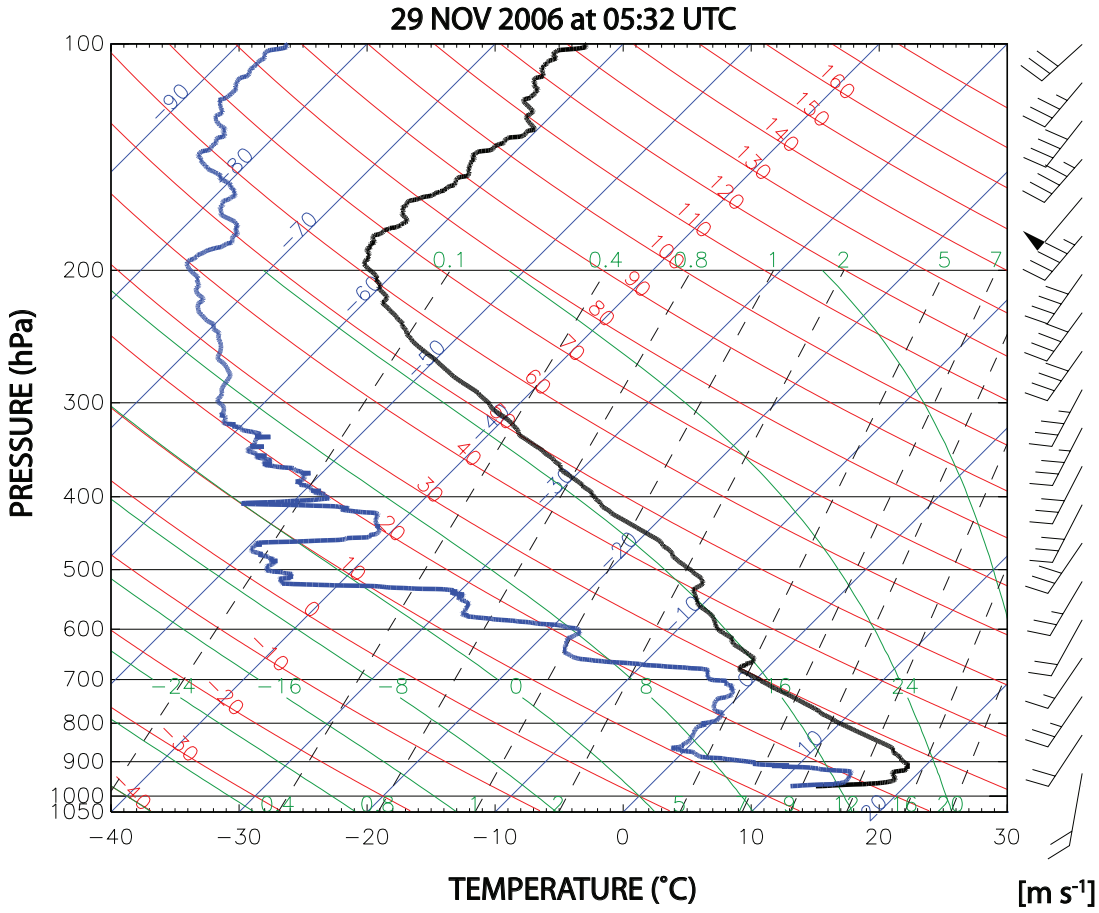


Fig. 10: Sounding taken from the Lamont, Oklahoma, ARM site valid at 0532 UTC 29 November 2006. The bold black line is the vertical temperature profile and the bold blue line is the vertical dewpoint temperature profile. Wind speed and direction are indicated by the wind barbs to the right using the following convention for speed: half-barb, 2.5 m $s^{-1}$; full-barb, 5 m $s^{-1}$; flag, 25 m $s^{-1}$.

FIGURE 11

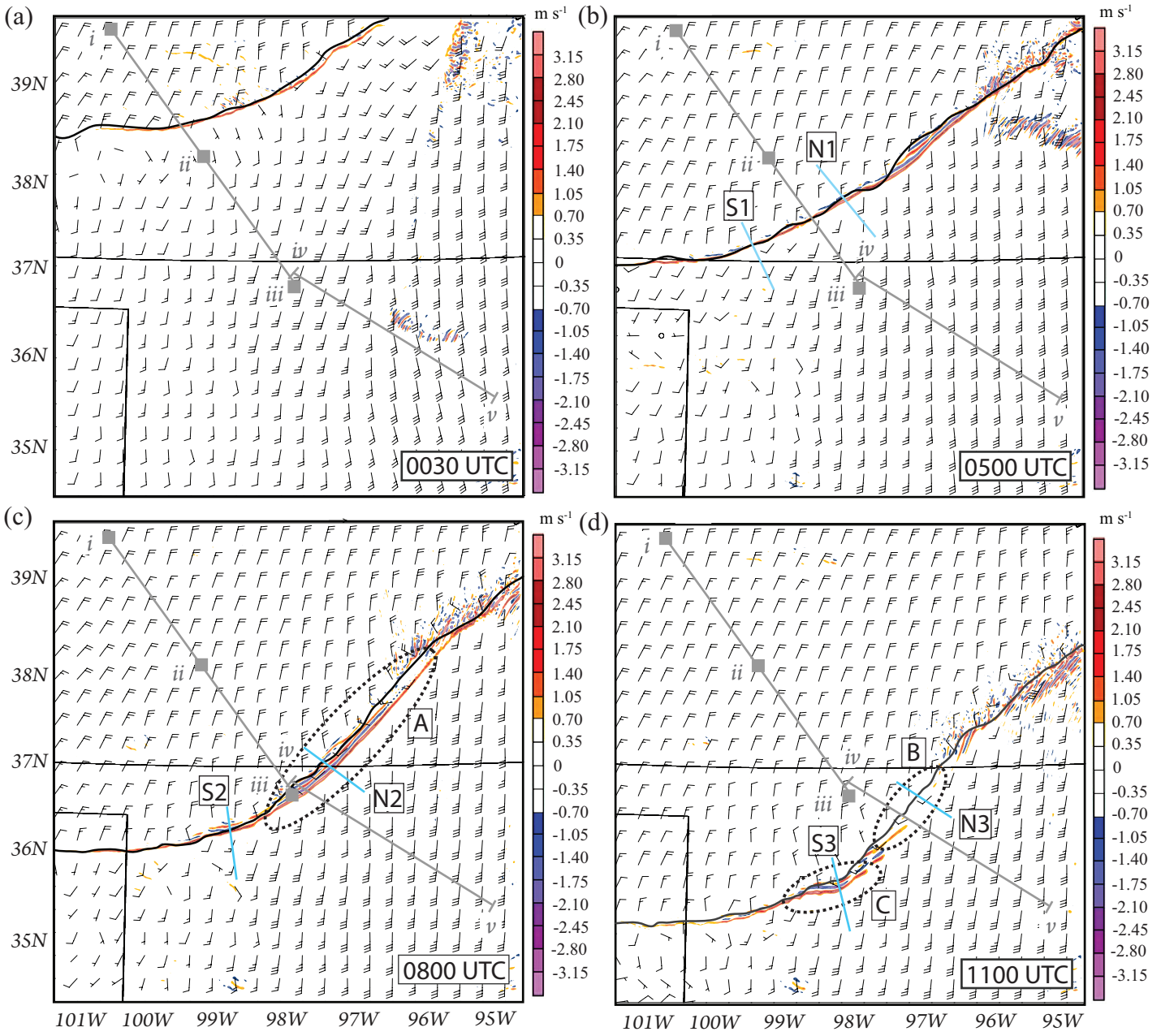


Fig. 11: Shaded vertical velocity (m $s^{-1}$) at 1 km ASL from Domain 2 of model simulation valid at (a) 0030 UTC, (b) 0500 UTC, (c) 0800 UTC and (d) 1100 UTC 29 November 2006. Labeled regions (A, B, C) are discussed in the text. Bold black line is the smoothed surface 290 K isentrope indicative of the leading edge of the surface thermodynamic boundary. Grey lines show cross-sections from Figure 2 and are discussed in Figures 12-14. Wind barbs represent horizontal wind speed and direction at 0.5 km ASL with one full barb corresponding to 5.0 m $s^{-1}$. Light blue lines mark the location of the north (N) and south (S) series of cross-sections shown in Figure 15.

FIGURE 12

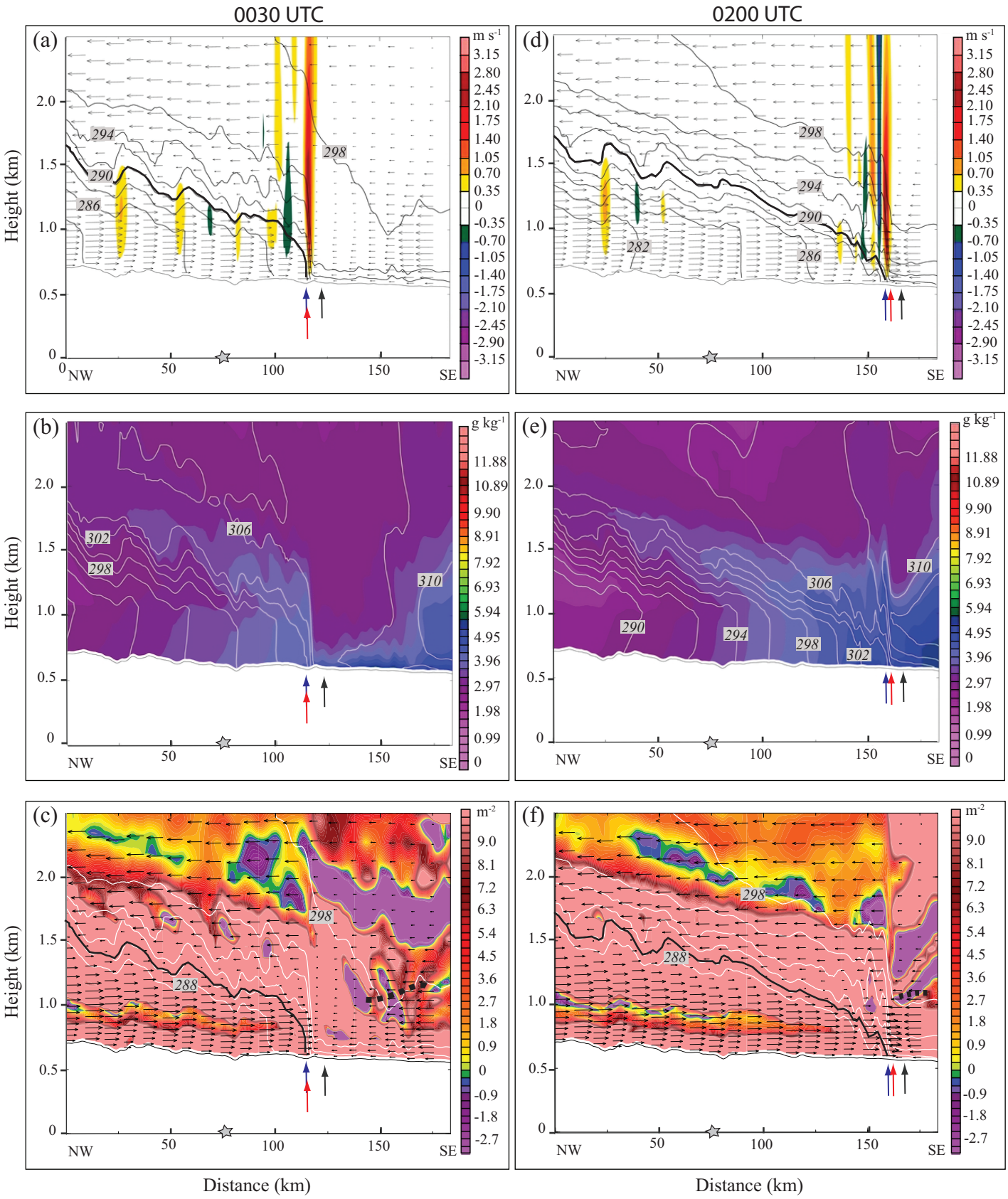


Fig 12: Vertical cross-section of WRF model output from Albert, KS to Red Rock, OK (along line *i-ii* in Fig. 11). Left hand column is valid at 0030 UTC and right hand column is valid at 0200 UTC 29 November. Panels (a) and (d) show potential temperature (solid black) contoured every 2 K, along cross-section horizontal wind vectors and vertical motion shaded every 0.35 m $s^{-1}$ according to scale at right. Bold black line is the 290 K isentrope. Panels (b) and (e) show mixing ratio in g $kg^{-1}$ shaded every 0.25 g $kg^{-1}$ and equivalent potential temperature (white) contoured every 2 K. Panels (c) and (f) show the Scorer parameter shaded every $0.3x10^{-6}$ $m^{-2}$ with all values less than $-3x10^{-6}$ saturated with solid purple and all values greater than $10^{-5}$ saturated in pink and potential temperature contoured in solid white from 288 K to 298 K. Horizontal black arrows indicate direction and magnitude of along cross-section wind component with longest arrow corresponding to a 12 m $s^{-1}$ wind speed. Blue arrows indicate position of surface thermodynamic boundary (290 K isentrope) and red arrows indicate position of surface wind shift. Bold black dashed lines indicate the critical level ahead of the bore / TB system. Vertically-oriented black arrows point to region characterized by a low-level stable layer and grey star indicates location of Larned, Kansas in the cross-section.

FIGURE 13

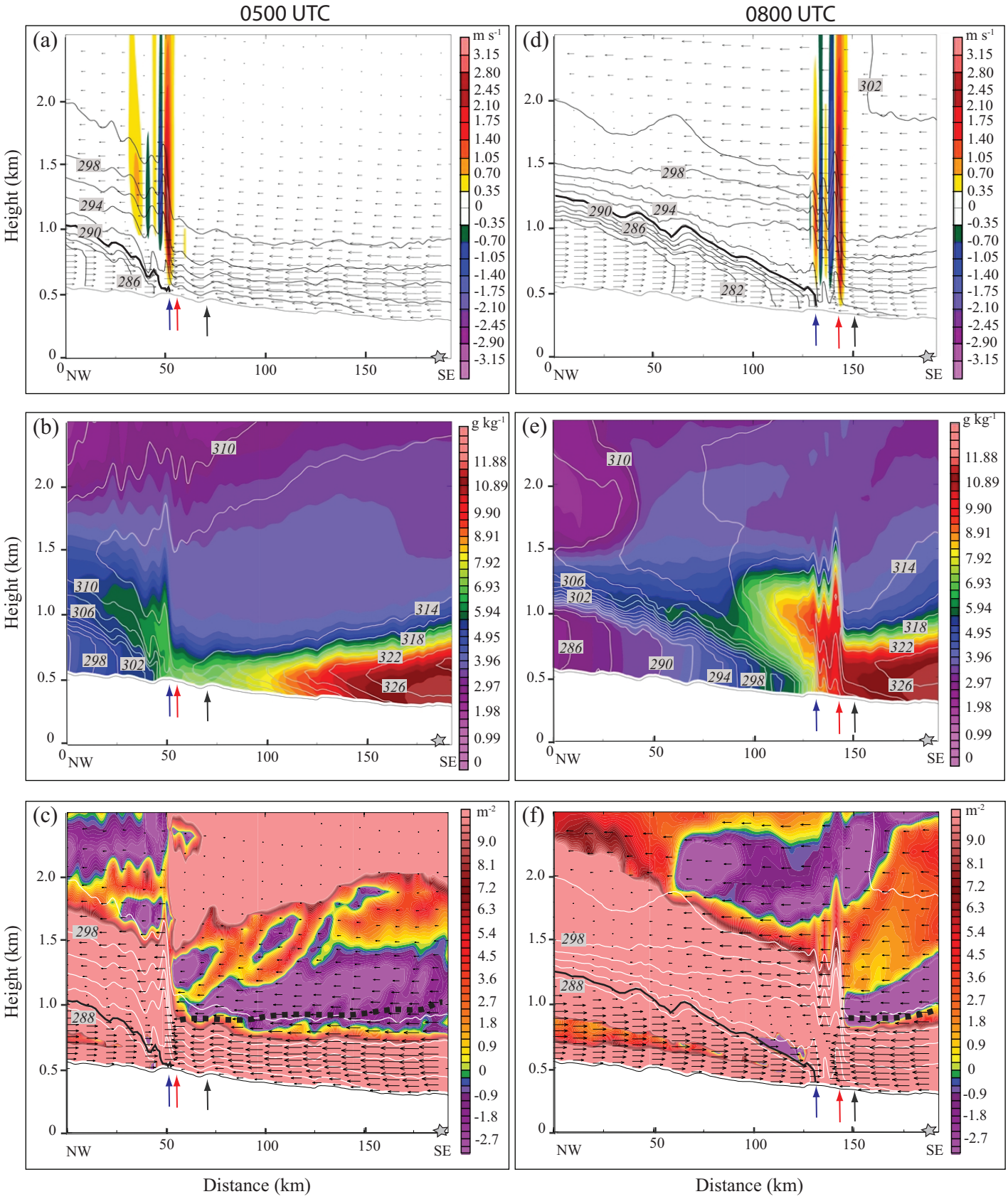


Fig 13: WRF simulation output along cross-section *ii-iii* in Figure 11. Data shown is the same as Figure 12, but left column displays data valid at 0500 UTC and right column shows data from 0800 UTC 29 November. Longest along cross-section arrows correspond to a 17 m $s^{-1}$ wind speed. Grey star indicates location of Lamont, Oklahoma in the cross-section.

FIGURE 14

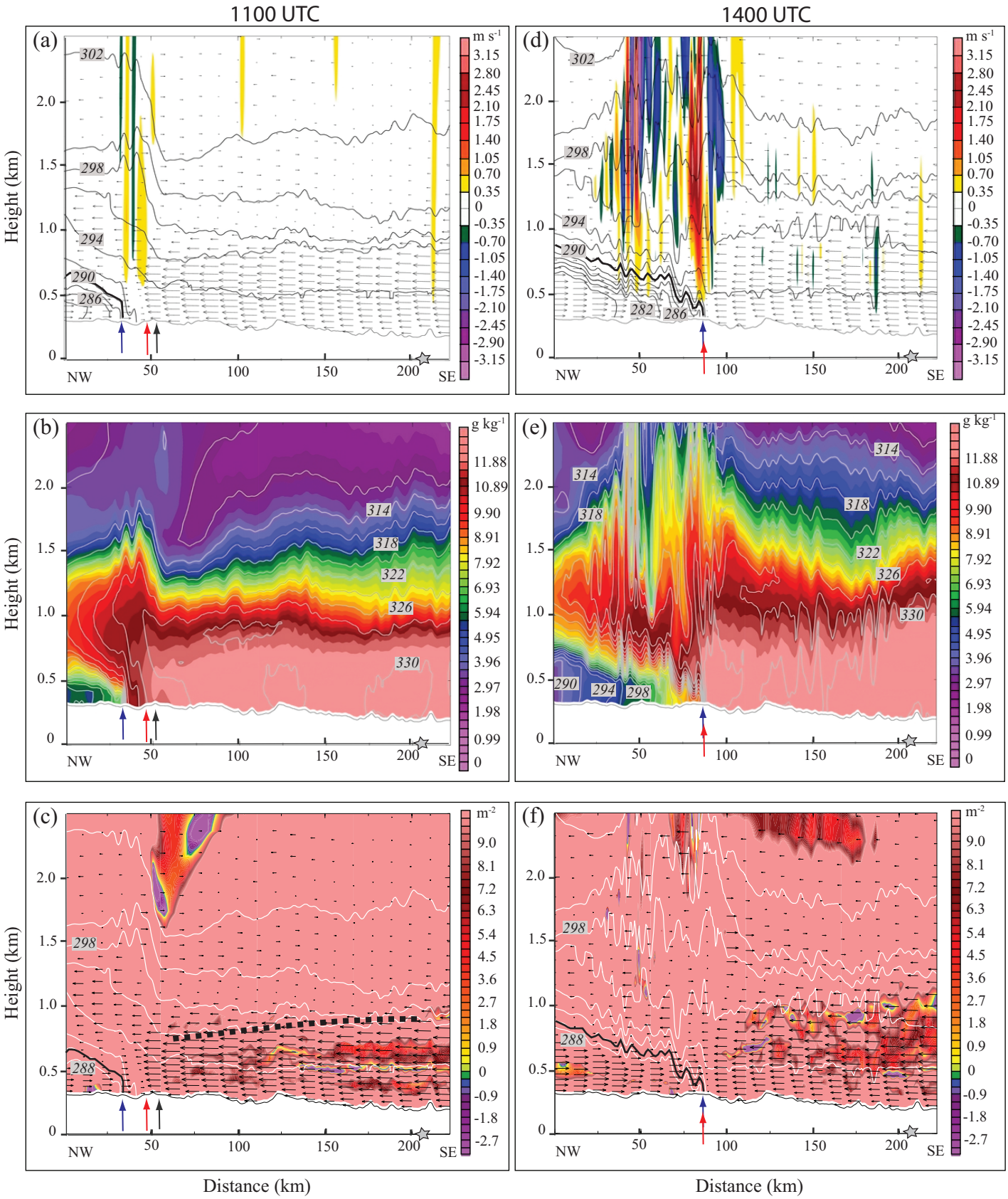


Fig. 14: WRF simulation output along cross-section *iv-v* in Figure 11. Data shown is the same as Figure 13, but left column displays data valid at 1100 UTC and right column shows data from 1400 UTC 29 November. Longest along cross-section arrows correspond to a 13 m $s^{-1}$ wind speed. Grey star indicates location of Okmulgee, Oklahoma in the cross-section.

FIGURE 15

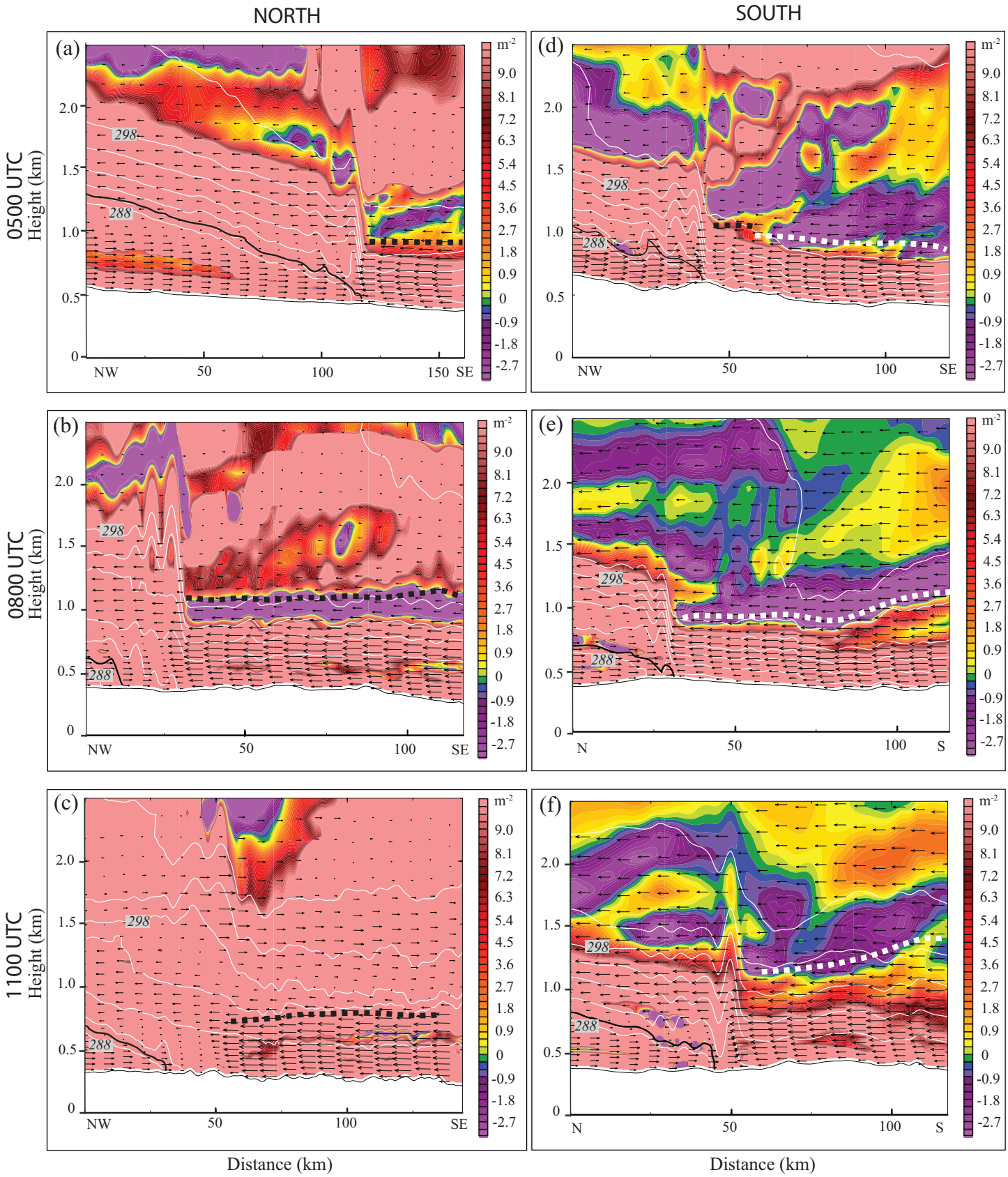


Fig. 15: Vertical cross-sections of WRF model output from N series (left column) and S series (right column) cross-sections in Figure 11. Panels (a)-(c) are taken along N1, N2 and N3 in Fig. 11 respectively. Likewise, panels (d)-(f) are taken along S1, S2 and S3 in Fig. 11 respectively. Panels (a) and (d) (top row) are valid at 0500 UTC, panels (b) and (e) (middle row) are valid at 0800 UTC and panels (c) and (f) (bottom row) are valid at 1100 UTC 29 November 2006. All panels show the Scorer parameter shaded as in Figs. 12-14. Potential temperature is contoured in white with the 290 K isentrope (indicating the position of the surface thermodynamic boundary) contoured in black. Horizontal black arrows indicate direction and magnitude of along cross-section wind component with longest arrows corresponding to 12 m $s^{-1}$ in the left column and 17 m $s^{-1}$ in the right column. Bold black dashed lines indicate the critical level ahead of the bore / TB system. Bold dashed white lines indicate the base of a layer where $U = c_{bore}$ (critical layer).